



Geochemistry, Geophysics, Geosystems®



RESEARCH ARTICLE

10.1029/2024GC011769

Footwall Geology and Deformation at Flip-Flop Mid-Ocean Ridge Detachment Faults: 64°35'E Southwest Indian Ridge (SWIR)

S. Mahato¹  and M. Cannat¹ 

¹Institut de Physique du Globe de Paris, UMR 7154, CNRS, Université Paris Cité, Paris, France

Key Points:

- Deformation is brittle, with horizons of semi-brittle serpentinite gouge controlled by the availability of hydrous fluid during deformation
- Local corrugations and antithetic faults indicate along-axis strength contrasts in young flip-flop oceanic detachment fault (ODF) and footwall
- Observations indicate a broad ODF damage zone with fault splays linking around hm-thick phacoids of less deformed serpentinitized peridotite

Supporting Information:

Supporting Information may be found in the online version of this article.

Correspondence to:

S. Mahato,
souradeep.mahato@pm.me

Citation:

Mahato, S., & Cannat, M. (2025). Footwall geology and deformation at flip-flop mid-ocean ridge detachment faults: 64°35'E Southwest Indian Ridge (SWIR). *Geochemistry, Geophysics, Geosystems*, 26, e2024GC011769. <https://doi.org/10.1029/2024GC011769>

Received 16 JUL 2024

Accepted 7 JAN 2025

Author Contributions:

Conceptualization: S. Mahato, M. Cannat
Data curation: M. Cannat
Formal analysis: S. Mahato
Funding acquisition: M. Cannat
Investigation: S. Mahato, M. Cannat
Methodology: S. Mahato, M. Cannat
Project administration: M. Cannat
Software: S. Mahato, M. Cannat
Supervision: M. Cannat
Validation: S. Mahato, M. Cannat
Visualization: S. Mahato, M. Cannat
Writing – original draft: S. Mahato
Writing – review & editing: S. Mahato, M. Cannat

Abstract Using bathymetry and ROV dives, we investigate two successive flip-flop detachment faults (D1 active, D2 older) in the near-amagmatic 64°35'E region of the SWIR. Kilometer-sized benches on the upper slopes of D1 footwall form the D1 degraded breakaway. Scarps at the top expose the D2 fault zone with deformed serpentinitized peridotite, sigmoidal phacoids, planar fractures, and serpentinite microbreccia/gouge horizons. Two ROV sections of the D1 footwall show contrasting deformation styles, corresponding to distinct morphological domains, which relate to contrasting fault and footwall strength. One section documents corrugations, outcrops dominated by sigmoidal phacoids, and planar fractures with thin, discontinuous serpentinite microbreccia/gouge horizons. ROV dives in this corrugated domain show that NNE-trending km-spaced ridges and WNW-trending narrow benches in the shipboard bathymetry correspond, respectively, to broad undulations (mega-corrugations) of the D1 fault and to several antithetic minor normal faults (cumulated horizontal offset of ~285 m). The other section, lacking corrugations, broad ridges, and antithetic fault, has thicker and more continuous serpentinite microbreccia/gouge horizons, indicating a weaker fault. The abundance of such weak gouges probably reflects hydrous fluid availability during deformation. We link mega-corrugations in the western domain and km-scale lobes of D1 emergence to a broad detachment damage zone with up to ~600 m-thick mega-phacoids of less deformed serpentinitized peridotite. Small antithetic normal faults in the corrugated domain are interpreted as due to bending forces in the D1 footwall. Our findings highlight the three-dimensional, non-planar structural and morphological variability of the exhumed D1 detachment fault zone along the ridge-axis.

Plain Language Summary Along certain areas of mid-ocean ridges, seafloor spreading is mainly accommodated by large-offset (>10 km) normal faults known as oceanic detachment faults (ODFs), and volcanic activity is limited. The footwalls of these ODFs expose mantle-derived rocks (e.g., serpentinitized peridotite) on the seafloor. ODFs are categorized into two types: those forming in magma-robust conditions (e.g., along the northern Mid-Atlantic Ridge and some areas of the Southwest Indian Ridge [SWIR]) and those forming in nearly amagmatic conditions (e.g., 62°40'E, 64°35'E SWIR region). While magma-robust ODFs are well studied, we present for the first time detailed geological and structural analyses of two nearly amagmatic, alternate polarity (flip-flop) ODFs: D1 (active) and D2 (older), from the 64°35'E SWIR, using underwater mapping and robotic exploration. Our findings show that (a) flip-flop ODFs have substantially broader fault damage zones (at least ~600 m) than more magma-robust ODFs, with the highest strain horizons (up to ~8 m thick) dominated by foliated and cataclastic serpentinite gouge, controlled by hydrous fluid availability during deformation; and (b) the active D1 ODF's exhumed footwall and fault zone has a three-dimensional, non-planar structural and morphological variability, which we attribute to variations of fault and footwall strength along the ridge.

1. Introduction

Oceanic detachment faults (ODFs) accommodate a part of the plate divergence in sections of slow-spreading ridges that have a reduced magma supply, typically but not exclusively, at the end of ridge segments (Buck et al., 2005; Cann et al., 1997; Cannat et al., 2008; Escartín & Cannat, 1999; Escartín et al., 2008; Sauter et al., 2013; Smith et al., 2008). Along the north Mid-Atlantic Ridge (MAR), areas of asymmetrical accretion dominated by ODFs account for ~50% of the ridge length (Escartín et al., 2008) or ~25% of the newly accreted seafloor (Cannat et al., 1995). These ODFs have large offsets (~5–35 km) and lifespans of ~1–2.6 myr (Tucholke et al., 1998). Exhumed fault surfaces are typically gently dipping (<20°) with dome-shaped topography and

© 2025 The Author(s). Geochemistry, Geophysics, Geosystems published by Wiley Periodicals LLC on behalf of American Geophysical Union. This is an open access article under the terms of the [Creative Commons Attribution License](https://creativecommons.org/licenses/by/4.0/), which permits use, distribution and reproduction in any medium, provided the original work is properly cited.

commonly bear corrugations aligned parallel with the spreading direction (Cann et al., 1997; Tucholke et al., 1998), analogous to continental detachment faults (John, 1987). Although detachments may initiate as linear and continuous faults extending over 20 km along-axis, active MAR dome-shaped ODF footwalls typically span <20 km along-axis (Escartín et al., 2017; MacLeod et al., 2009; Smith et al., 2006, 2014). These ODFs root at depths of ~7–12 km with a high dip (~60–70°) as revealed by micro-earthquakes (deMartin et al., 2007; Parnell-Turner et al., 2017). Corrugated ODF footwalls exhume variably deformed serpentinized peridotite, gabbroic, basaltic, and lesser diabase lithologies (Cannat et al., 1995, 1997; Casey, 1997; Dick et al., 2008; Kelemen et al., 2007; MacLeod et al., 2002; Mével et al., 1991; Picazo et al., 2013; Schroeder et al., 2007), while the hanging wall typically exposes volcanic seafloor (Cannat et al., 2006; MacLeod et al., 2009; Smith et al., 2006).

Sample studies (e.g., Atlantis Bank, Dick et al., 2000; 16.5°N MAR, Casini et al., 2021; 13°N MAR, Picazo et al., 2012) and numerical modeling (Olive et al., 2010) suggest that corrugated and domal ODFs root into a magma-infiltrated hot ductile domain. Deformation within these faults is primarily brittle to semi-brittle, localized in serpentine-talc-chlorite-amphibole greenschist facies assemblages with rare cataclasites (Bonnemains et al., 2017; Boschi et al., 2006; Dick et al., 2002; Escartín et al., 2003; Hansen et al., 2013; Picazo et al., 2012; Schroeder & John, 2004). Microbathymetry, remotely operated vehicle (ROV) dive observations and drilling of domal ODFs along the MAR show that while semi-brittle to brittle fault rocks may be found ~100 m or more below the corrugated fault surface (e.g., 13°20'N, Escartín et al., 2017; Atlantis Massif, Karson et al., 2006; 15°45'N, MacLeod et al., 2002), most deformation occurs in the upper 10 m of the exposed fault (Boschi et al., 2006; Karson et al., 2006; Schroeder & John, 2004). Additionally, ROV observations (Escartín et al., 2017; Karson et al., 2006) do not document several meters thick cataclastic domain below the exposed fault, contrasting with observations made at fossil ocean-continent transition (OCT) detachments (Picazo et al., 2013).

The easternmost region of the ultraslow-spreading SWIR (east of Melville Fracture Zone) is an end member of the global MOR system in terms of its low overall melt supply (Cannat et al., 1999, 2008; Minshull et al., 2006). It shows domal corrugated structures similar to MAR ODFs, over ~4% of the mapped area (Cannat et al., 2006). However, ~40% of the mapped area shows broad ridges that extend ~25–95 km parallel to the ridge axis (Cannat et al., 2006, 2019). These broad ridges form in nearly amagmatic spreading corridors between more volcanic domains and do not appear corrugated in shipboard bathymetry (Cannat et al., 2006). They expose mostly (~90%) serpentinized peridotite (Sauter et al., 2013). Both flanks of these ridges are interpreted as exhumed footwalls of opposite polarity (flip-flop) ODFs (Sauter et al., 2013). Compressional wave velocity models indicate that the upper part of the lithosphere (down to ~5 km bsf) in these smooth seafloor domains has geophysically defined crustal seismic velocity and density properties and probably consists of fractured and variably serpentinized peridotites with incipient magmatic bodies (Corbalán et al., 2021; Momoh et al., 2017; Robinson et al., 2024). Studies of partially serpentinized dredged samples indicate that these flip-flop detachments root into a nearly amagmatic semi-brittle to ductile domain of fresh peridotites, creating distributed zones of high-stress deformation and grain size reduction (Bickert et al., 2020, 2021).

This study focuses on the active D1 axial detachment at 64°35'E SWIR (Figure 1). It faces south and has been active for ~300 kyr, cutting through detachment D2, which had an opposite polarity and was active for ~1.5 myr (Cannat et al., 2019). Detachment D1 is therefore at an early stage of development. Its footwall faces sparsely volcanic to non-volcanic ultramafic seafloor on the hanging wall side (Sauter et al., 2013) with increasing magmatism in the form of isolated volcanic patches and ridges toward the west (Cannat et al., 2006). The Old City hydrothermal field, with spectacular carbonate-brucite chimneys, was discovered mid-slope of the axial valley wall (Lecoeuvre et al., 2021; Cannat et al., 2021; Figure 1b). Seismic reflectors interpreted as D1 detachment-related damage, which dips ~50° at ~5 km bsf, are imaged over a width of ~0.5–1.8 km below the base of the D1 footwall, suggesting that the detachment fault damage zone is broad (Momoh et al., 2017, 2020). Microseismicity is recorded down to ~15 km bsf beneath the axial valley floor, providing a minimum estimate for the local depth to the brittle-ductile transition (Chen et al., 2023). In contrast to what has been documented in MAR corrugated detachments (deMartin et al., 2007; Parnell-Turner et al., 2017, 2021), earthquakes are not focused along the fault zone and in the detachment footwall but also occur in the hanging wall. All these observations concur to suggest significant differences in the way deformation is accommodated and localized between the more common corrugated-volcanic spreading mode (Cannat et al., 2006) and the nearly amagmatic (i.e., nearly fully tectonic) flip-flop plate divergence mode identified in the eastern SWIR.

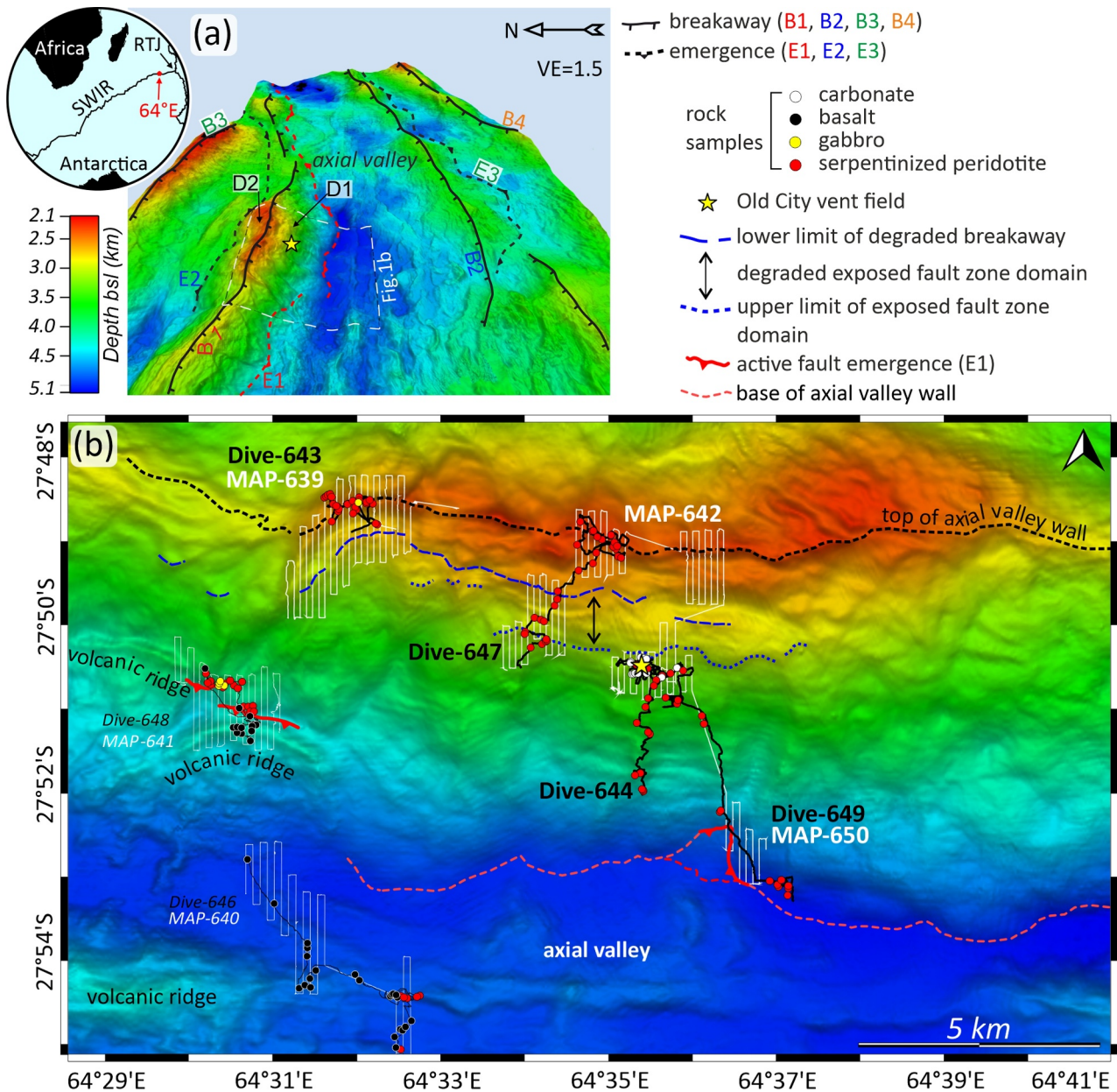


Figure 1. Regional context and location of ROV dives. (a) 3D view of shipboard bathymetry (view toward east) over the 64°35'E near axis region of the eastern SWIR. This view highlights the breakaways (B1–B4) and emergences (E1–E3) of recent axial detachments (Sauter et al., 2013). (b) Shipboard bathymetry in map view (location in a), focusing over the axial valley and the northern axial valley wall, corresponding, respectively, to the hanging wall and footwall of active detachment D1. Tracks of ROV microbathymetry surveys are shown as white lines, tracks of ROV exploration dives in black, and the primary lithology of recovered samples is indicated with circular-colored symbols. ROV dives analyzed in this paper are numbered in bold. The two blue dashed lines are limits traced based on combining bathymetry and dive geological observations: long dashes for the base of the degraded breakaway domain and short dashes for the base of the degraded exposed fault zone domain (see text).

This paper presents the first map to outcrop and sample-scale study of the geology and deformation of SWIR flip-flop detachment faults. We use shipboard bathymetry, microbathymetry, and seafloor exploration videos acquired with the ROV (Remotely Operated Vehicle) VICTOR during the ROVSMOOTH 2017 cruise of RV *Pourquoi Pas?* The ROV dive observations take us from the emergence of the D1 detachment in the axial valley to the top of its footwall (top of the northern axial valley wall, Figure 1b). Our results document the anatomy and along-axis structural variability of the exposed D1 and D2 fault zones and provide original observational constraints on the deformation behavior of flip-flop mid-ocean ridge detachment faults.

2. Data and Methods

The shipboard bathymetry data (50 m grid spacing) used in this study were acquired during the ROVSMOOTH cruise onboard RV *Pourquoi Pas?* with a RESON 7150 multibeam echosounder (12 KHz frequency, beam opening angle of 151°, and a ship velocity of 6 knots). High-resolution bathymetry data (1 m grid spacing) used in this study were acquired during three dives of ROV Victor 6000 (dives 639, 642 and 650; Figure 1b) using a RESON 7125 echosounder mounted on the ROV frame, with an operating frequency of 400 kHz, a beam opening angle of 120°, a velocity of ~0.3 m/s, and an altitude ~50 m above the seafloor. Ultra-short baseline ROV positioning was poor due to the steep and irregular slopes. Processing of the data was therefore carried out (with the Caribes 5.0 software @Ifremer) track by track and maps used in this paper result from a track-by-track manual adjustment of these grids with the GlobalMapper software (@BlueMarble).

We used the high-resolution topography to interpret seafloor geology derived from ROV exploration videos and sampling from dives 643, 644, 647, and 649 (from D1 emergence to the top of D1 footwall; Figure 1b). We illustrate dive observations with a selection of video snapshots (field of view: ~15–20 m in the foreground unless specified otherwise). We used ROV heading direction, pan, and camera tilt to estimate the orientation of structural planes such as rock cleavage and schistosity. We also used side scan sonar data acquired in the area with the TOBI (Towed Ocean Bottom Instrument; Sauter et al., 2013). Map scale data integration and analyses were carried out using the Global Mapper software (@BlueMarble). ROV exploration dives 643, 644, 647, and 649 produced seafloor video footage along four different dive tracks (~30 km total) and recovered 118 rock samples. Of these, 105 samples come from confirmed outcrops (as opposed to talus). We performed a preliminary microstructural study of a small selection of serpentinite gouge samples using optical and scanning electron microscopy (SEM; performed on an EVO MA10 Zeiss, a high-resolution imaging platform housed at Institut de Physique du Globe de Paris, France).

3. Results

The footwall of the active D1-detachment (the south-facing axial valley wall; Figures 1b and 2a) has a relief of ~2,600 m relative to the axial valley floor. Within the axial valley wall between 64°34'E and 64°37'E longitudes, the overall slope ranges from ~20° to 24°. Local steeper slopes, however, reach up to ~30° over a 2 km north-south stretch and ~25° over a 3 km north-south stretch in the lower half of the axial valley wall (Figure 1b). East of 64°37'E, the overall slope of the axial valley wall decreases, ranging from ~15° to ~20°, with the shallowest slopes of 15° observed at the easternmost extent of the study area (Figure 1b). D1 emerges from the seafloor at or near the base of the axial valley wall. ROV observations are too scarce to locate this emergence precisely at the regional scale. In Figures 1 and 2, we thus trace the bottom of the axial valley wall, except where dive data confirms the actual location for the emergence of the D1 fault zone. ROV dives considered in this study (643, 647, 644, and 649; Figure 1b) recovered mostly variably serpentinized and deformed peridotites (90 out of a total of 118 samples), with minor gabbros (1 sample in dive 643) and hydrothermal carbonates from the Old City hydrothermal field (20 samples, dives 644 and 649). As will be shown, observations of the D1 footwall at three different scales, for example, shipboard bathymetry, microbathymetry, and ROV exploration dives, point to three domains with distinct morphology and tectonic structure. They are, from bottom to top (Figure 2c):

1. *The exposed fault zone (EFZ) domain*: it covers the lower slopes from north of the D1 emergence (~5,000 mbsl) up to a slope break that occurs at depths of ~2,700–~3,000 mbsl.
2. *The degraded exposed fault zone (DEFZ) domain*: it covers an intermediate domain of locally mostly concave-down slopes with intermittent exposures of the exhumed D1 fault zone at depths ranging from ~3,000 to 2,650 mbsl.
3. *The degraded breakaway (DB) domain*: a ~700–1,500 m wide domain just below the top of the axial valley wall, characterized by several hectometers to kilometer-sized benches that represent slid-down blocks of the degraded D1 breakaway (Figures 2b and 2c).

In the following sections, we describe the geology and the structure of each domain, from the base of the wall upward to the top of the axial valley wall, where the seafloor formed by the previous D2 detachment fault is exposed (Figure 1b).

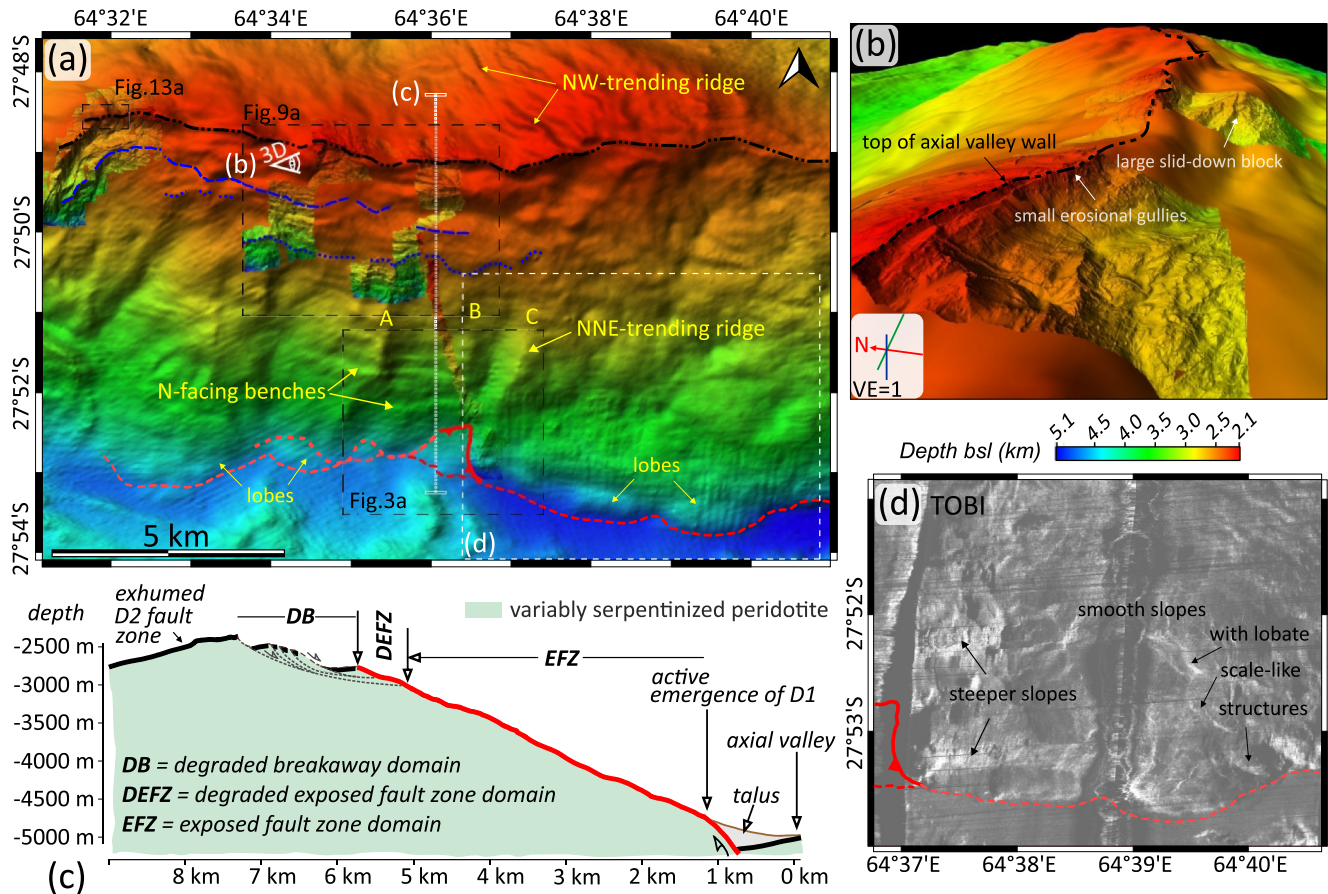


Figure 2. Map scale characteristics of the D1 footwall. (a) Microbathymetry for ROV dives 639, 642, and 650 overlain on shipboard bathymetry (color scale in b). Color scales for microbathymetry are as detailed in Figures 3a, 9a, and 15a (located by insets). Symbols for D1 emergence, base of degraded fault zone domain, bottom of degraded breakaway domain, and top of footwall, as in Figure 1b. Illumination from the 315°N direction emphasizes north-facing scarps, particularly in the bottom half of the wall. NNE-trending ridges A, B, and C are numbered as in Figure 3a. (b) Perspective view of the upper portion of the axial valley wall and the degraded breakaway region, located in a, showing hectometer to kilometer-scale slid-down blocks, rigid or internally deformed, and more recent and smaller scale erosional gullies in the steepest scarps. (c) Morpho-tectonic interpretation of a north-south cross-section (positioned in a) of the exhumed detachment fault (D1) footwall, no vertical exaggeration. (d) Seafloor reflectivity image (TOBI; Sauter et al., 2013; located in (a)), showing the smooth eastern lower slopes of the footwall, with lobate, scale-like structures and two regions of steeper slopes.

3.1. The Exposed Fault Zone (EFZ) Domain

The exposed fault zone domain has an average slope of $\sim 24\text{--}27^\circ$. It is structured by north-northeast trending ridges (Figures 1b and 2a) up to $\sim 150\text{--}300$ m high with wavelengths of $\sim 0.7\text{--}2$ km, labeled “A,” “B,” and “C” in Figures 2a and 3a. Between these ridges, the topography is deeper and, in some instances (as in between ridges B and C; Figure 3a), is gully shaped. This ridge/gully (or ridge/lower topography) structure has about the same wavelength ($\sim 1\text{--}2.5$ km) as lobate domains visible near the base of the axial valley wall (Figure 2a). In Figure 3a, high-resolution bathymetry shows that the narrow gully between NNE-trending ridges B and C and the tip of ridge B corresponds to a recess between two lobate domains at the bottom of the wall. In addition to this ridge/lower topography structure, the EFZ domain displays several E to ESE trending lineaments, characterized by narrow (up to ~ 160 m wide) slope breaks or benches in shipboard bathymetry (labeled #1 to #4 in Figure 3a). Some of these lineaments (e.g., those shown in Figures 3b and 3c) are traceable up to ~ 4.5 km laterally (Figures 2a and 3a). Microbathymetry reveals that these lineaments correspond to north-facing antithetic fault scarps a few meters high (Figures 3b and 3c), some of which offset recent talus (Figure 3c). Two additional types of north-northeast trending lineaments that can only be seen in the microbathymetry data: corrugations ($\sim 1\text{--}\sim 30$ m high and up to ~ 400 m long; Figures 3a–3c) and faint undulations of the seafloor (less than 1 m high and up to 140 m-long; Figure 3b). These structures and the local geology from observations made during ROV dives 649 and 644 (Figure 3a) are described below.

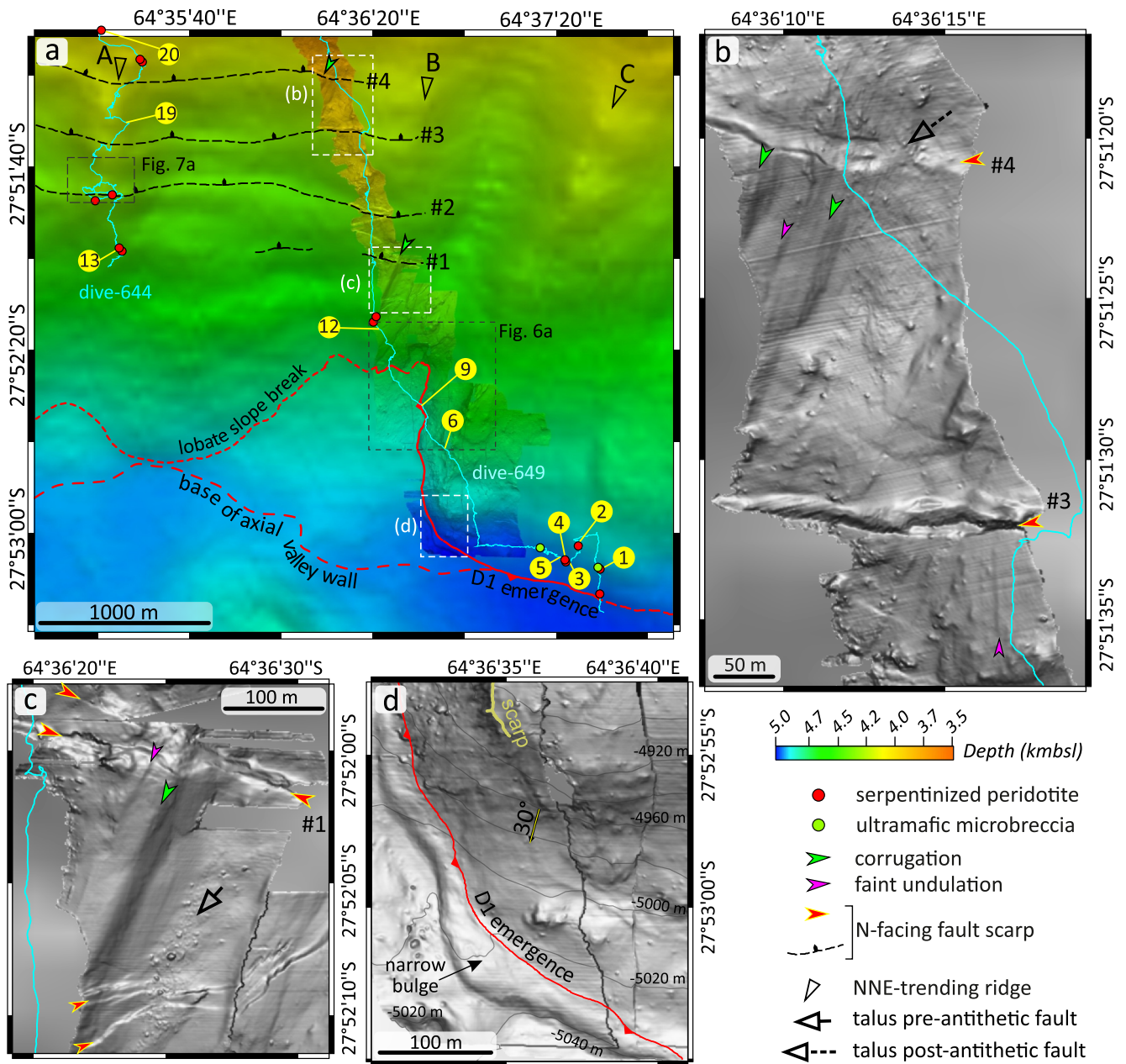


Figure 3. Bathymetric map of the lower slopes of the D1 detachment footwall, located in Figure 2a. (a) Microbathymetry (map 650; located in Figure 1b) overlain on shipboard bathymetry, same depth scale. Red and green dots show the location and lithology of the samples collected in these lower slopes along the tracks of dives 644 and 649. Numbers in yellow circles correspond to the location of seafloor video snapshots shown in Figures 4, 5, and 8. Other video snapshots from dives 644 and 649 are located and shown, respectively, in Figures S1 and S2 in Supporting Information S1. Panels (b–d) are gray-shaded details of the microbathymetry located in (a).

Dive 649 starts at a depth of $\sim 5,085$ m at the bottom of the axial valley wall. High-resolution topographic/bathymetry data was unfortunately not acquired at this location due to a technical problem, but dive observations are consistent with the high-resolution topographic data acquired ~ 1 km further west (Figure 3d). A slope break, transitioning from 5 to 10° below to $\sim 30 \pm 5^\circ$ above, is marked by a ~ 5 m high, ~ 15 – 50 m wide bulge, with northward-facing slopes of $\sim 25^\circ$ – 35° . This structure is analogous to the hanging wall cut-offs observed at the $13^\circ 20'$ and $16^\circ 35' N$ active MAR detachment faults (Escartín et al., 2017; Smith et al., 2014). We interpret this slope break as a trace of the emergence of the active D1 detachment fault. In the area of Figure 3d, this trace curves inward and upward to the north, diverging from the base of the axial valley wall (Figure 3a). In the side-scan sonar (TOBI) image (Sauter et al., 2013), the narrow bulge and its adjacent slope break coincide with a ~ 130 m wide

lobate band (Figure 2d) of acoustically bright seafloor (ABS). Additionally, two distinct bands of ABS are observed, characterized by locally steeper slopes. The first is more rectilinear, oriented east-west and ~300 m wide, occurs at depths of ~5,060 to 5,015 mbsl (Figures 2a and 2d) and was crossed during dive 649 (Figure 1b). The second is ~350–400 m wide and located upslope at depths of ~4,500 to 4,250 mbsl (Figures 2a and 2d). Other features of the TOBI record in these lower axial valley wall slopes are scaly shaped narrow higher backscatter patches that extend ~400–500 m in length and trend NW-SE (Figure 2d). Two of these higher backscatter patches in the eastern part of the TOBI coverage correspond to lobate topography at the base of the wall.

Geological observations made near the base of the axial valley wall at the beginning of ROV dive-649 show lightly sedimented south-dipping planar surfaces that extend several tens of meters along the slope (Figures 4b and 4c).

These planar surfaces correspond to meter-scale alternations of blocky serpentinized peridotite and horizons of foliated breccia and microbreccia. Outcrops are covered by a thin iron-manganese crust that is commonly eroded off, showing the bluish-white tint of the brecciated intervals (Figures 4a–4d). The talus of iron-manganese crust-free rubble also suggests recent local erosion of these lower slopes (photo no. 2 in Figure S2 in Supporting Information S1). In situ ROV sampling of the brecciated intervals (Figure 4a) yields fragile gouge samples with angular, sub-rounded, and elongated clasts of serpentinized peridotite and serpentinite in a foliated matrix made of sheared serpentine (Figures 4d and 4g). In thin sections, gouge and microbreccia intervals display foliated microshear domains with a fine matrix of serpentine fibers with both a shape and a crystallographic preferred orientation (Figures 4d–4f). These fibers crystallized during the deformation at the expense of serpentinite microclasts (Figure 4g). Therefore, the deformation mechanisms involved were likely semi-brittle.

In the field, the serpentine gouge and microbreccia horizons are <1 m (Figure 4c) to ~8 m-thick (Figure 4a). The intervening layers of blocky, more massive serpentinized peridotite are cut by a dominant, parallel family of fractures and by secondary sets of fractures, the most developed being more steeply south-dipping fractures, which we interpret as Riedel brittle shears (Figures 4c and 5a). A closer look at a recently eroded scarp in one of these blocky horizons (Figure 5a) shows a ~0.5 m-thick greenish-white serpentinite shear zone subparallel to the upper surface of the outcrop (other horizons of this serpentine gouge plus microbreccia material form the local slope, visible in the background of Figure 5a). Serpentinized peridotite blocks above the shear zone are slightly rotated along antithetic sheared fractures (Figure 5b). These fractures are also filled with whitish-sheared serpentine material (Figure 5b). Serpentinized peridotites below the shear zone are distinctly schistose over at least ~0.5 m (Figure 5a). The schistosity also dips south but more gently than the shear zone.

Together, these observations are consistent with a top-to-south shear displacement. Several steeper south-dipping fractures also cut the serpentinized peridotites below the shear zone, similar to those in the background of Figure 4c, some also lined by white serpentinite material (Figure 5a). Outcrops that offer a view to the north (orthogonal to the slope and the plate divergence direction) also locally show an anastomosing fault zone fabric with sigmoidal phacoids ~10–15 m-wide and ~4 m thick (Figure 5c). The sigmoid peripheral and the neck zones between two sigmoids commonly develop thin greenish-white gouge-bearing microbreccia intervals, whereas the sigmoid core is less deformed (Figure 5c).

In the deepest portion of NNE-trending ridge C and the adjacent gully (Figures 3d and 6a), the D1 emergence turns north and upward. The footwall, with WSW to SW-facing, ~30–35° slopes, emerges from a domain of shallower slopes (~13–19°) to the west that is covered by blocky talus (Figure 6a). Moving upslope along the dive 649 path, the outcrops are first barely emerging from the south-dipping slopes and exposing the same assemblage of blocky, fractured, and locally brecciated serpentinites and occasional bluish-white serpentinite gouge. After passing over the tip of ridge C and going toward the ~N-S trending emergence trace (Figures 3a and 6a), the topography is a bit rougher, with faint undulations that trend N27–N35°, probably related to the observed anastomosing fault fabric (Figures 6b and 6c). A massive serpentinized peridotite outcrop a few tens of meters to the east of the emergence shows slope parallel curved scaly fault planes (Figure 6d), discordant on an earlier set of meter-spaced, planar, south to southeast dipping fractures that recall those in Figure 4b, with a perpendicular set of secondary joints. Closer to the emergence, at location 9 (Figure 6a), a >1 m-thick interval of serpentinite gouge and microbreccia sits structurally above these fractured massive serpentinites and coincides with more gentle slopes (Figure 6e). To the north of location 9, a domain of smoother southwest-facing slopes was not explored during dive 649. It displays several faint ~N25 to N30° trending undulations in the microbathymetry, extending up to ~130 m (Figure 6a). These lineaments are not detected in the shipboard bathymetry but are very similar to

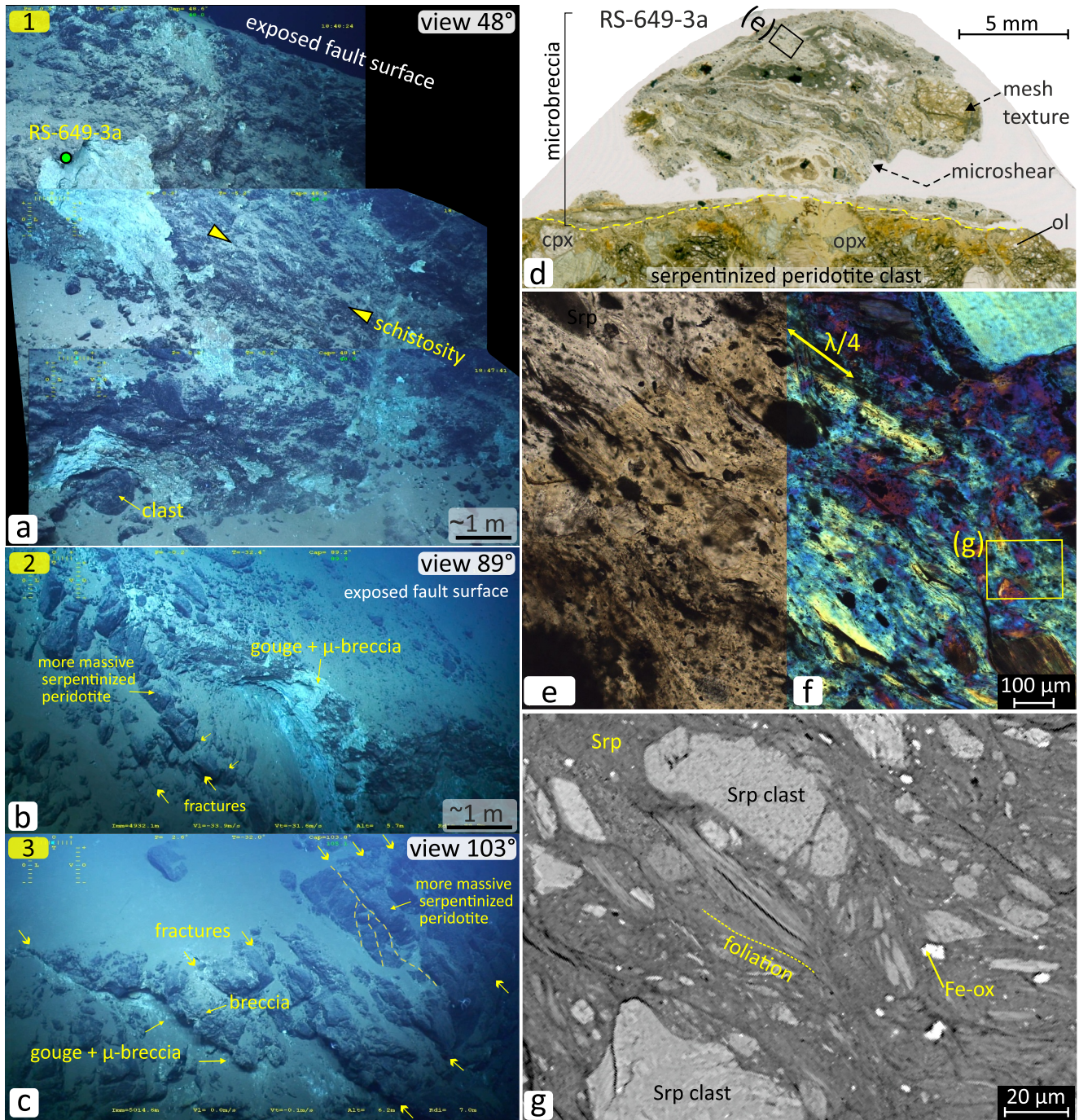


Figure 4. Lower slopes of the D1 detachment footwall. Selected ROV snapshots (numbers in yellow box in the upper left corner correspond to locations in Figure 3a and the numbers in the white box in the upper right corner correspond to the viewing direction from the north.), and microstructure of highly sheared sample RS-649-3a. (a) Photomontage of 3 ROV snapshots showing a ~8 m thick horizon of serpentinite gouge and microbreccia. The south-dipping planar surface at the top is the exposed fault surface. The outcrop has a rough schistosity parallel to this fault surface. Location of sample RS-649-3a is shown. (b) Side view of planar exposed fault surface with ~1 m of gouge/microbreccia over more massive serpentinitized peridotite with a set of sub-parallel fractures (dipping south ~30–45°). (c) Another side view shows that several meters below the main exposed fault surface (it is outside the view to the right; field of view ~12 m in foreground), some fractures are also lined with pale green gouge/microbreccia material. Also shown in the background of (c) are sets of conjugate steeper fractures in more massive serpentinitized peridotite. (d) Full thin section view of sample RS-649-3a (natural light) from gouge-microbreccia horizon in (a) shows a ~10 mm-thick microclast-bearing sheared domain, which corresponds to the pervasive schistosity of the outcrop in (a). (e) Closer view of a sheared interval in natural light, located in (d). (f) Detail of (e) in polarized light with an additional wave plate showing a strong crystallographic preferred orientation of the sheared serpentine. (g) Backscattered electron (BSE) image located in (f) shows elongated, angular to subrounded serpentinite (Srp) microclasts in the sheared serpentine matrix.



Figure 5. Selected ROV snapshots, dive 649, lower slopes of the detachment footwall. Numbers in yellow in the upper left corner correspond to locations in Figure 3a. (a) Outcrop is made of blocky serpentinized peridotites with a gouge and microbreccia shear zone, ~50 cm-thick, gently south-dipping, overlying more massive, yet locally schistose serpentinized peridotite, with set of conjugate, steeper south-dipping fractures, some filled with whitish sheared serpentinite material. (b) Detail of shear zone with slightly rotated serpentinized peridotite blocks separated by sheared fractures also filled with white sheared material. Geometry is consistent with top-to-south normal displacement. (c) Here, the gently south-dipping exposed fault surface is made of serpentinized peridotites with anastomosing fractures delimiting sigmoidal phacoids. Small amounts of whitish gouge and microbreccia material are found in the neck and peripheral domains.

the small-scale corrugations described in high-resolution bathymetric maps of MAR corrugated detachments (Escartín et al., 2017; Parnell-Turner et al., 2018; Smith et al., 2014).

ROV dive 649 then continues across a domain of gentle south-facing slopes (~20°), covered by talus generated by a horseshoe-shaped erosional scarp, ~100 m high (Figure 6a). The microbathymetry along this scarp offers a view of multiple ~5–10 m high steps (Figure 6a). Although not explored with the ROV, these steps could correspond to the edges of several stacked and anastomosing fault surfaces. Further to the west, the D1 emergence, with slopes of ~33–35°, shows undulations at wavelengths of ~20–50 m (Figure 6a). Moving upward onto the tip of NNE-trending ridge B (Figure 3a), the high-resolution bathymetry shows NNE-trending east-facing slope breaks or scarps (Figure 6a), revealing a faint slope-parallel planar fabric that could also correspond to stacked anastomosing fault surfaces (Figure 6a). The most prominent slope break is ~6–12 m high and ~300 m long. The slope (26–27°) above and to the west of this slope break bears a faint N20° trending lineament that can be followed for ~27 m (Figure 6a). At a depth of ~4,530 m, ROV dive 649 crosses the southern end of a prominent corrugation, ~30 m high, ~140 m wide, that trends N21° and extends at least ~450 m (Figure 3c). Further upslope, the high-

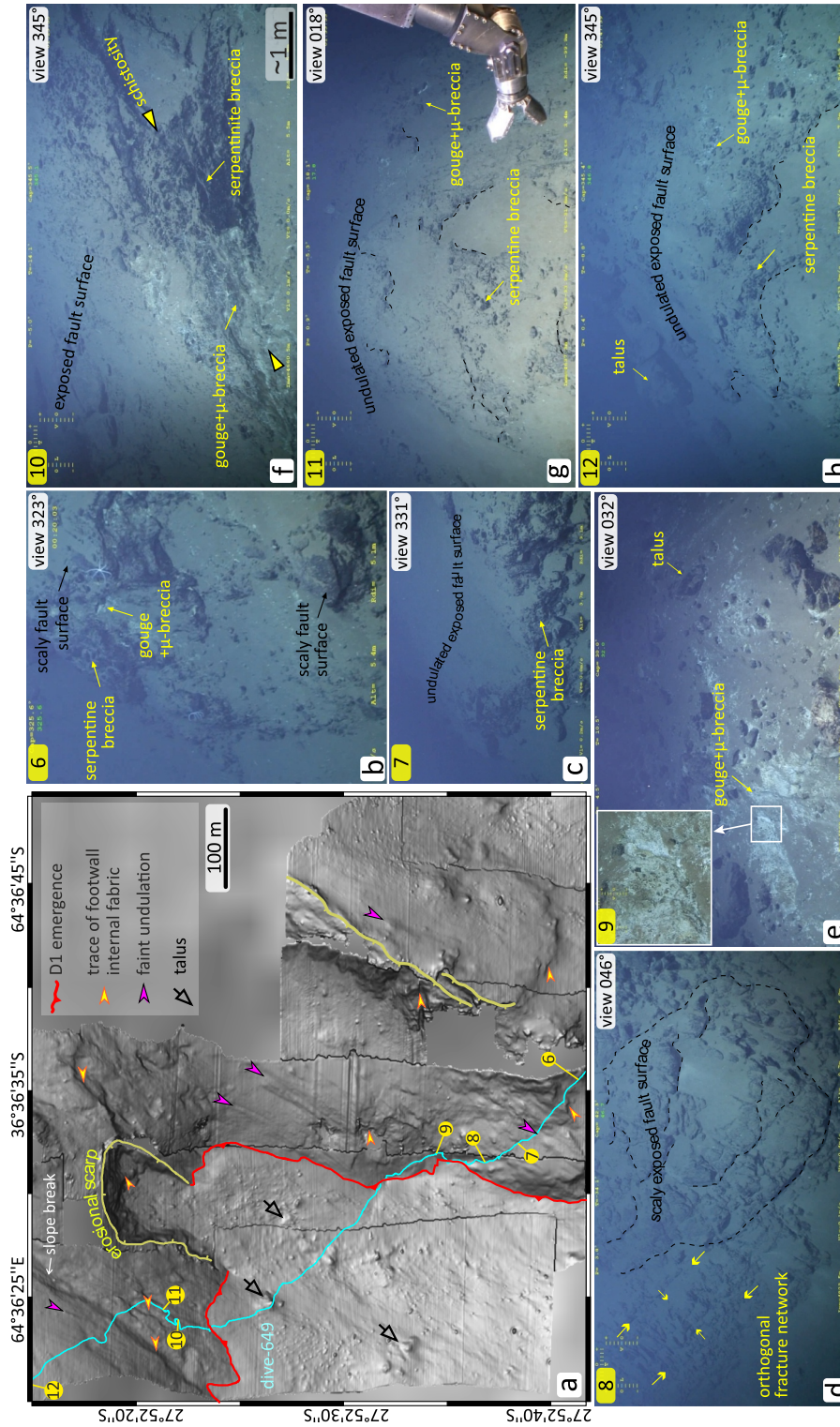


Figure 6. Lower slopes of axial valley wall along the track of ROV dive 649; located in Figures 1b and 3a), shaded gray scale. Numbers in yellow circles correspond to the location of seafloor video snapshots shown in panels (b–h); field of view ~15–20 m in foreground except in (f). Other video snapshots from dive 649 are located and shown, respectively, in Figures S1 and S2 in Supporting Information S1. To the west, the exhumed fault surface emerges with a 25–35° south or southwest-facing slope from more gentle slopes that expose talus deposits. This fault surface locally bears faint undulations. Slope breaks and erosional scarps provide windows into the internal fabric of the fault zone; planar features with an apparent dip to the south. In (b) and (c), the exposed fault surface dips S to SSW in brecciated serpentinitized peridotite with occasional gouge-bearing microbreccia intervals. In (d) and (e), the exposed fault surface dips to the SW. In (d), it consists of scaly fractures in a relatively massive serpentinitized peridotite outcrop with prominent preexisting orthogonal fractures (the apparent dip of the dominant set is to the south). In (e), the exposed fault surface has a gentler dip and is made of at least 1 m of serpentinite gouge and microbreccia. In (f), a small erosional scarp shows at least 0.5 m of microbreccia over schistose serpentinitized peridotite beneath the planar exposed fault surface. In (g) and (h), the exposed fault surface corresponds to at least 1 m of brecciated serpentinite and is undulated (amplitude >1 m over 15–20 m). Scaly and tear-apart structures on these undulated fault planes are consistent with down-dip, undulation-parallel normal displacement.

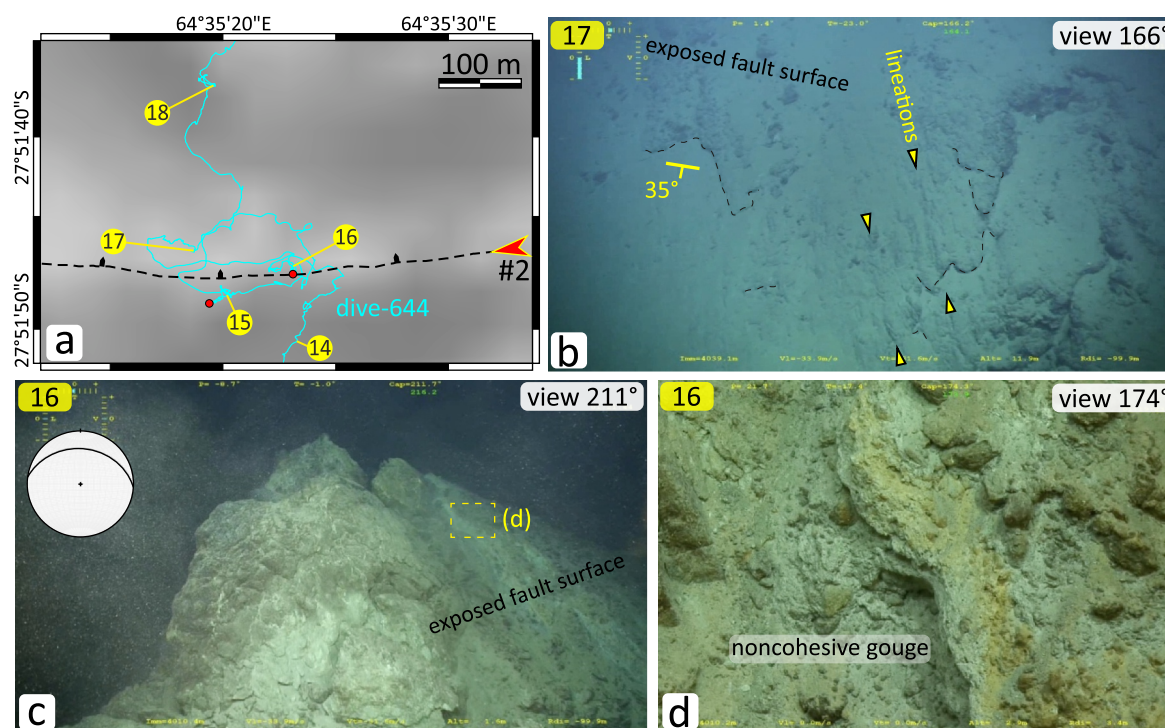


Figure 7. North-facing antithetic fault scarp along the track of dive 644. (a) Map view of dive 644 track around antithetic fault scarp #2 (located in Figure 3a). Numbers in yellow circles correspond to the location of seafloor video snapshots shown in panels (b–d; field of view ~15–20 m in foreground except in (d)), and in (b) the scarp exposes a north dipping fault plane, with steep northwest-trending lineations and scaly and tear-apart structures consistent with normal displacement. (c) Another view of the north-dipping fault plane, lined with at least 1 m of non-cohesive gouge in (d).

resolution bathymetry documents two other faintly corrugated exposed fault zone regions at depths between 3,080 and 4,020 m, with lineaments trending N357° and N16°, respectively (Figure 3b). These corrugated middle-lower slopes are light to heavily sedimented. Outcrops are characterized by slope parallel, planar (Figure 6f), or curved and undulating fault surfaces (Figures 6g and 6h) with local occurrences of greenish-white serpentine gouge (Figures 6f–6h). Scarps that offer a view below these fault surfaces typically show a few decimeters of gouge and microbreccia, followed by ~1 m of extensively brecciated serpentinite overlying more massive yet fractured serpentinitized peridotite (Figure 6f).

A striking characteristic of the microbathymetry in these middle-lower slopes of the axial valley wall is the occurrence of several N, NNE, or NNW-facing scarps/slope breaks that offset the exposed detachment surface (Figures 3b and 3c) and some of the recent talus (Figure 3c). Some of these scarps correspond to the N-facing benches visible in the shipboard bathymetry (Figure 3a). In the high-resolution bathymetry, they range in height from ~3 m or less for the NE-trending array that offsets the talus in Figure 3c, and ~20 m for the scarp numbered #3 in Figures 3a and 3b. Scarp #2 (Figure 3a) was explored during ROV dive 644 (Figure 7). It exposes a north-dipping fault plane with down-dip to NNW-trending striations and scaly tear-apart structures that indicate normal, down-to-north displacement (Figure 7b). Beneath this fault plane are a few decimeters of a non-cohesive, yellowish serpentinite gouge and microbreccia formation (Figures 7c and 7d). Using ROV navigation and immersion data, we calculate an average local dip of 35° for this antithetic fault plane. Assuming a fault dip of 35° for scarps #1 to 4 in Figure 3a would amount to a cumulated horizontal throw of ~76 m.

ROV dive 644 explores the NNE trending ridge A from a depth of ~4,320 m upward. The geology there is rockier than that documented by ROV dive 649 over the same depth range on the western flank of ridge B (Figure 3a). Outcrops of serpentinitized peridotites display a range of fracturation facies: from planar fractures, spaced by 1 m or more, with sets of perpendicular joints (Figure 8b) to more pervasively fractured outcrops with decimeter to several meter-spaced planar and sigmoidal fractures (Figures 8a, 8c, and 8e), and occasional decimeter-thick intervals of the green-white serpentine gouge formation (Figures 8a and 8c). These facies can be interpreted in terms of increasing strain. In several instances, the exposed D1 fault surface corresponds to the development of

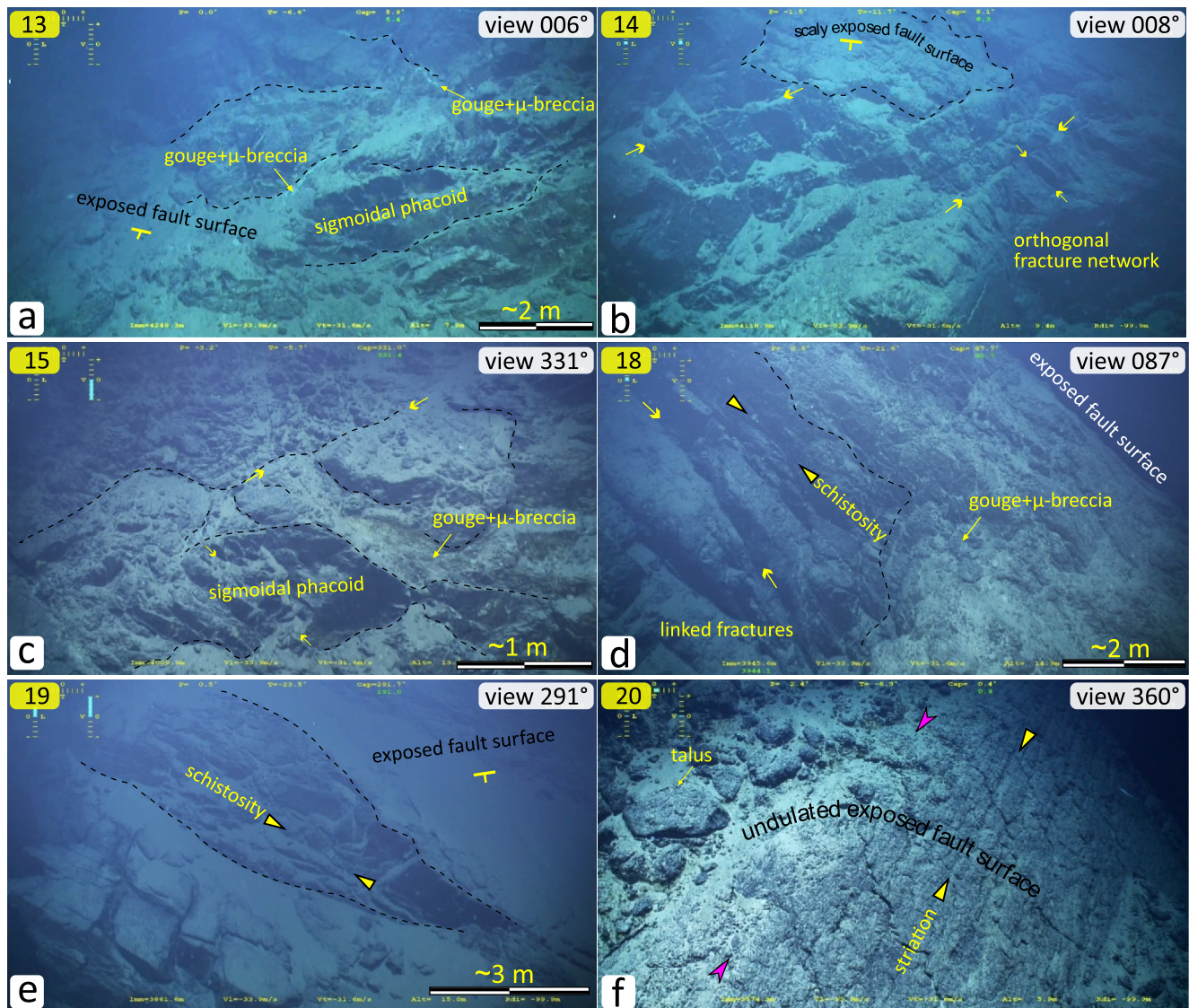


Figure 8. Selected ROV snapshots along NNE-trending ridge A, dive 644. In the upper left corner, numbers in yellow correspond to locations in Figures 3a and 7a. In (a), (b), and (c), a dominant set of fracture dips to the S or SW. In (a) and (c), these fractures define sigmoidal phacoids and are locally outlined by gouge and microbreccia (up to ~50 cm-thick in panel c). In (b), these fractures are planar, defining an orthogonal network, and similar to Figure 6d, there is a discordant, later, south-dipping scaly fault plane in the background. In (d), an erosional scarp reveals the deformation beneath the south-dipping planar fault plane, with ~1 m of gouge and microbreccia, over serpentinized peridotite with concordant schistosity and sigmoidal phacoids. Panel (e) is on the east flank of ridge A, and exposed fault planes have a dominant, slope-parallel, southeast dip. They isolate decameter-long flat sigmoidal phacoids in serpentinized peridotite that has a platy schistosity/cleavage. (f) Shows an undulated striated exposed fault surface (undulation trends NNE, field of view ~10 m).

tight concordant fractures or schistosity (Figures 8d and 8e) with or without gouge and microbreccia intervals that transition to meter-spaced sigmoidal fractures ~5 m below (Figure 8d). In other instances, decameter-scale slope-parallel fault surfaces are discordant on the least deformed fractured facies (Figure 8b). In terms of geometry, the dominant dip of decameter-scaled exposed planar, undulated, and sigmoidal fault surfaces along ridge A varies from southwest-ward (locations 13, 14, and 15; Figures 8a–8c) to southward (location 18; Figure 8d), then southeast-ward on the eastern side of ridge A (location 19; Figure 8e). This suggests that the ridge-like topography is due to kilometer-scale undulations (large corrugations) of the exposed fault surface.

NNE-trending ridge A continues up to ~3,300 mbsl into the upper slopes of the EFZ domain just below the Old City vent site (Figure 9a). NNE-trending ridges B and C (Figure 2a) and two other ridges to the west of ridge A (A' and D; Figure 9a) extend up to similar depths. Overall, the topography in the upper slopes of the EFZ domain is

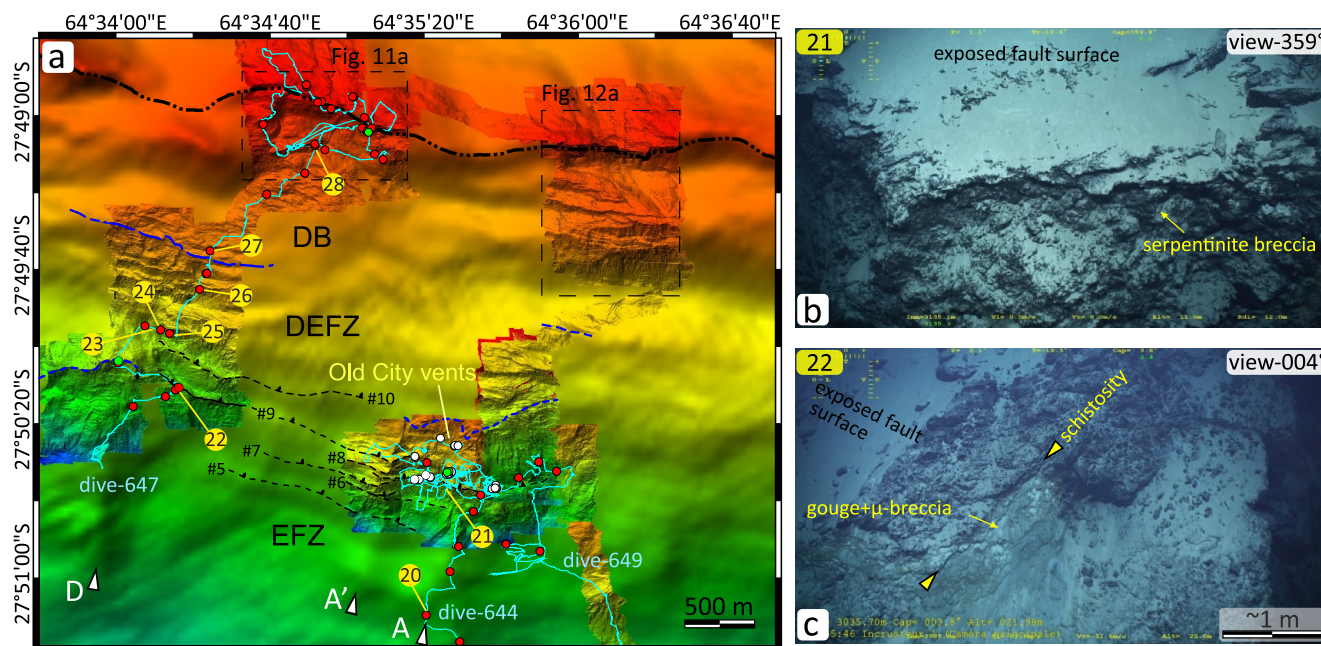


Figure 9. Middle and upper slopes of the axial valley wall along the tracks of ROV dives 644, 647, and 649. (a) Microbathymetry (maps 642 and 650; located in Figures 1b and 2a) overlain on shipboard bathymetry. The depth scale is the same as in Figure 1. Numbers in yellow circles correspond to the location of seafloor video snapshots shown in panels b and c (field of view $\sim 15\text{--}20\text{ m}$ in foreground) and Figure 10. Other dive video snapshots from dives 644, 647, and 649 are located and shown in Figures S2 and S4 in Supporting Information S1. Blue (short dashed) and purple (long dashed) lines are proposed limits between the EFZ (exposed fault zone) and DEFZ (degraded exposed fault zone) and between the DEFZ and the DB (degraded breakaway) domains. A, A', and D are NNE-trending ridges, as in Figure 2a. Dashed black lines numbered 5 to 10 are north-facing, antithetic normal fault scarps. (b) and (c) are selected ROV snapshots showing exposed D1 fault surfaces in the upper slopes of the EFZ domain, near the Old City vents in (b), and further to the west along dive 647 in (c).

more chaotic than in the lower regions, with evidence for substantial mass wasting in the form of hectometer-sized landslide lobes (Figure 9a and Figure S3 in Supporting Information S1). However, outcrops of decameter-scale fault surfaces remain common (Figures 9b and 9c). As in the deeper parts of the EFZ domain, these fault surfaces are associated with brecciated, locally schistose serpentinite, with occasional decimeter-scale horizons of pale green serpentinite gouge (Figure 9c). Other serpentinite outcrops are more massive, displaying the now typical planar to sigmoidal fracture patterns (photos no. 3–8 in Figure S4 in Supporting Information S1).

North-facing, antithetic fault scarps that can be followed a few km in the shipboard bathymetry also remain common in the upper EFZ slopes (Figure 9a). Most active vents of the Old City hydrothermal field (Lecoivre et al., 2021) are located along scarp #8. High-resolution bathymetry in the Old City area reveals at least 6 such scarps, not all of which are detectable in the ship bathymetry. These scarps, which are up to $\sim 30\text{ m}$ high and spaced $\sim 20\text{--}70\text{ m}$ apart, offset Ridge A'. Collectively, assuming fault dips of 35° (as documented for scarp #2, Figures 7a and 7b), these antithetic minor faults would amount to a cumulated horizontal throw of $\sim 209\text{ m}$.

3.2. The Degraded Exposed Fault Zone (DEFZ) Domain

The DEFZ domain is well constrained by microbathymetry and dive observations between $64^\circ 33'\text{E}$ and $64^\circ 37'\text{E}$ longitudes (Figures 1b and 9a) but poorly defined to the west and east of these bounding longitudes, respectively. This domain is characterized by a stepped, chaotic, and locally concave-down topography, with steeper slopes than the degraded breakaway located above and gentler slopes ($\sim 18\text{--}24^\circ$) than in the EFZ ($\sim 24\text{--}27^\circ$) domain below (Figure 9a and Figure S7d in Supporting Information S1). The limit between the two structural (DEFZ and EFZ) domains coincides with a slope break at $\sim 3,000$ to $3,100\text{ mbsl}$ and aligns with the northern end of the NNE-trending ridges (Figure 9a). Some of the N-facing antithetic fault scarps extend into the DEFZ domain. Observations made during ROV dive 647 show that south-facing DEFZ slopes expose the same combination of decameter-scale, breccia-lined fault surfaces (which might, in most cases, be decameter-sized blocks (Figures 10a and 10d)), and fractured serpentinites (Figures 10b and 10c) as the EFZ domain. Most fractures dip toward the

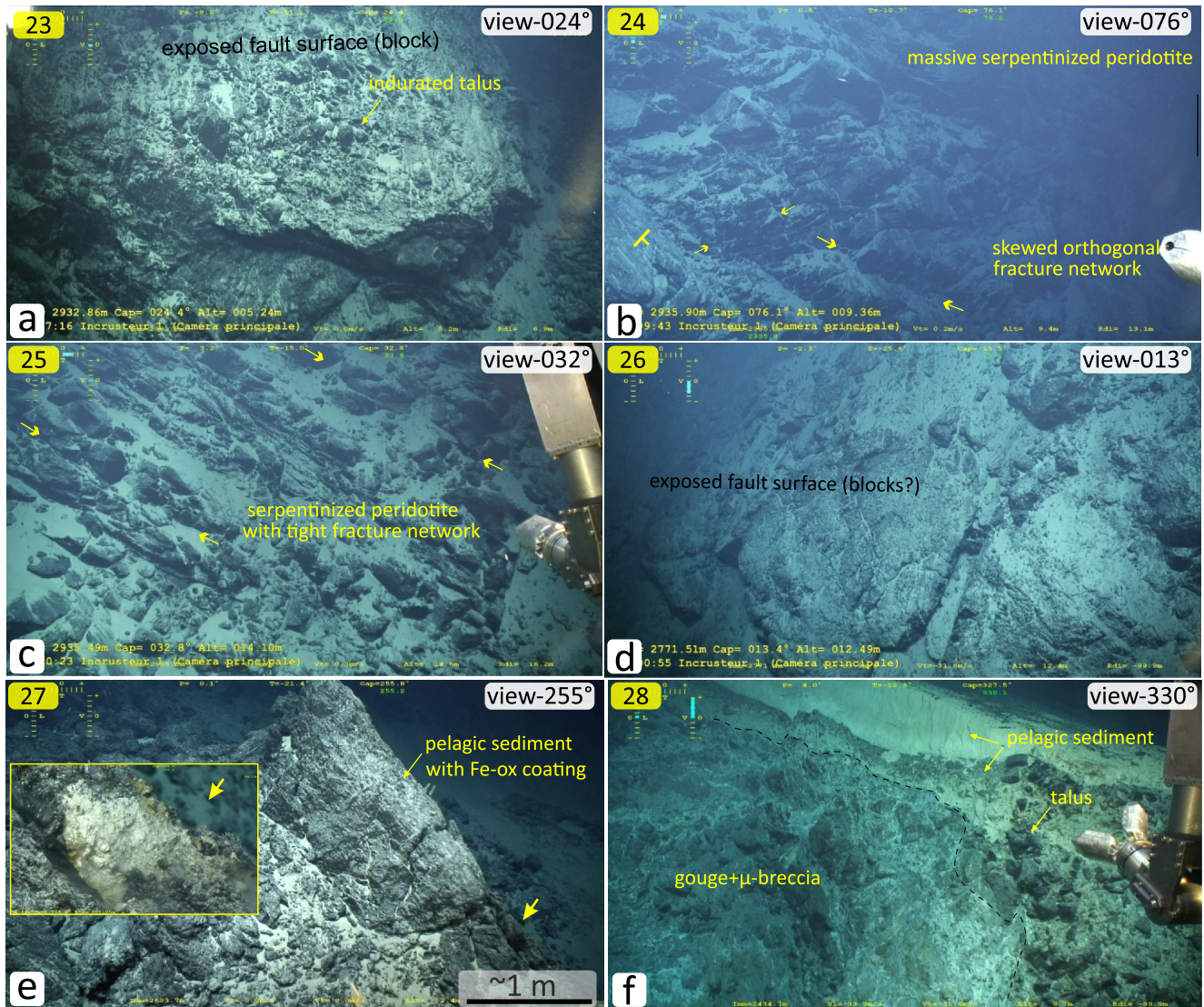


Figure 10. Selected ROV snapshots in the DEFZ (degraded exposed fault zone; a to d) and DB (degraded breakaway; e and f) domains, dive 647. Numbers in yellow in the upper left corner correspond to locations in Figure 9a. (a) Exposed fault surface is probably a large block covered with semi-indurated talus. (b) Large outcrop of massive serpentinized peridotite with conjugate fractures: the secondary set of north-dipping fractures may have been rotated from orthogonality due to normal displacement on dominant, south-dipping fractures. (c) Another large outcrop, with tight subparallel and linked southeast-dipping fractures. (d) Exposed fault surfaces, blocks, or outcrops. (e) First encounter with thick (>1.5 m) and iron-manganese oxide-coated, semi-indurated pelagic sediments characteristic of the exposed D2 fault surface (see Figure 11b). (f) Foliated serpentinite gouge and microbreccia with ~1 m-thick cover of pelagic sediment on top of a slid-down block just south of the top of the axial valley wall (see Figure 11a).

south. They form networks ranging from several -meter spaced with conjugate joints (Figure 10b) to decimeter-scaled with local schistose intervals (Figure 10c). The last probable outcrop of an exposed fault surface was encountered at a depth of 2,771 mbsl (Figure 10d), and the south/south-southeast dipping fault zone structure was identified at 2,653 mbsl (photo no. 29 in Figure S4 in Supporting Information S1). North-facing slopes and the depressions associated with the antithetic scarps as well as south-facing detachment fault scarps are covered by pelagic sediments and talus, including fresh talus without sediment cover (photo no. 26 in Figure S4 in Supporting Information S1).

3.3. The Degraded Breakaway (DB) Domain

At 2,603 mbsl, ROV dive 647 encountered a 1 to 2 m-thick outcrop of semi-indurated pelagic sediment, with a cm-thick crust of iron-manganese oxide (Figure 10e), very similar to outcrops found over the top of the axial

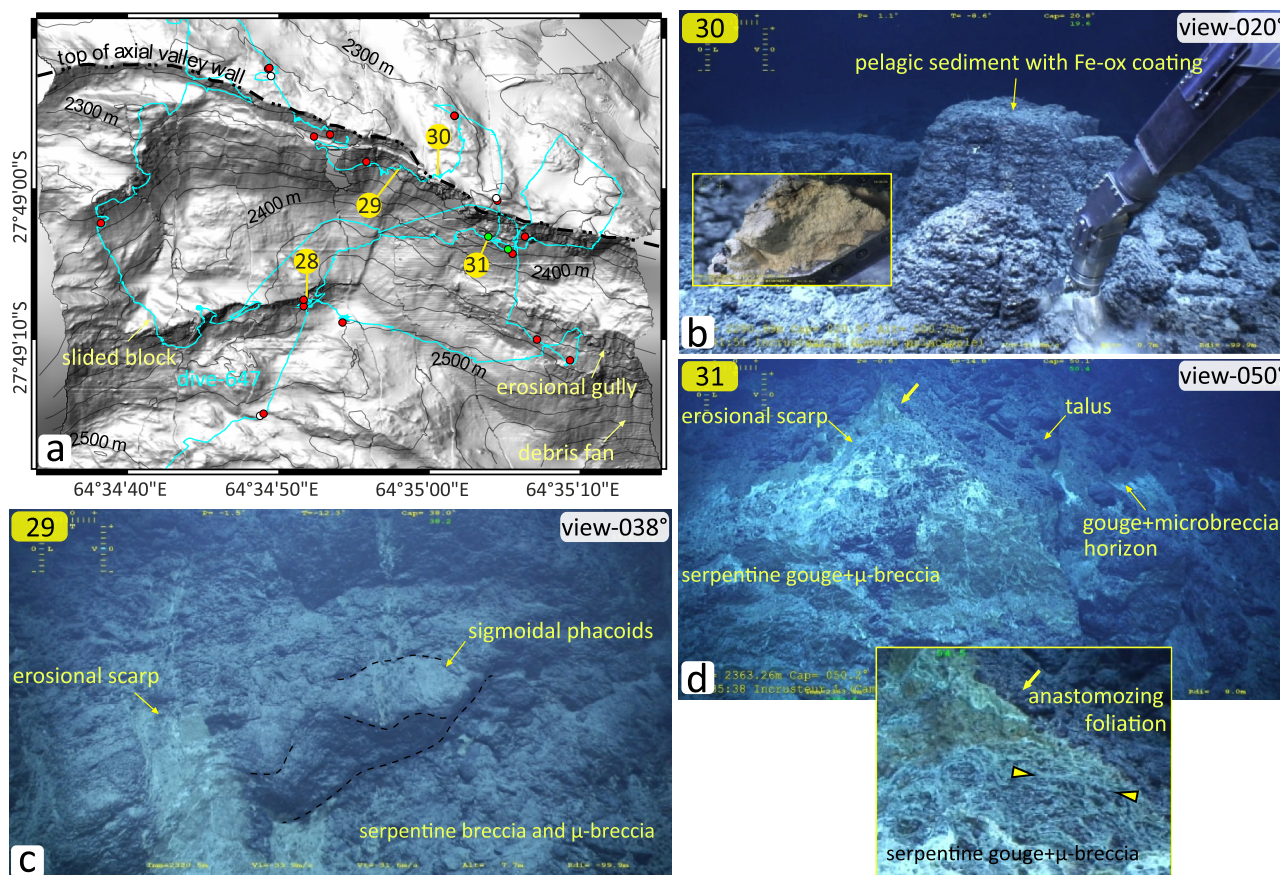


Figure 11. D2 exposed fault surface explored during dive 647 along the top of the axial valley wall. (a) Shaded microbathymetry (map 642, located in Figure 9a) shows the track of dive 647 and the location of rock samples. Numbers in yellow circles correspond to the location of seafloor video snapshots shown in panels (b–d; field of view ~15–20 m in foreground). Other dive video snapshots from dive 647 are located and shown in Figures S3 and S4 in Supporting Information S1. (b) Thick (>1.5 m) and iron-manganese oxide-coated semi-indurated pelagic sediments on top of the wall (exposed D2 fault surface). (c) Large outcrop of serpentinite breccia and microbreccia with north-dipping schistosity and sigmoidal phacoids, ~40 m below the exposed fault surface. (d) Large outcrop of serpentinite breccia, microbreccia, and gouge, with north-dipping and anastomosing foliation, ~55 m below the exposed fault surface.

valley wall (Figure 11b). This old (based on the thickness of the oxide crust) and thick sedimentary formation signify the location of the deepest slid-down block of degraded breakaway material. Topographically, there is no clear break with the DEFZ domain below: the transition occurs within the region of gentle concave downward slopes that extend between ~2,500 and ~2,770 mbsl at the latitude of dive 647 (Figures 2c and 9a; Figures S7a and S7d in Supporting Information S1). Above this region of gentle concave downward slopes, the uppermost portion of the wall is structured in a series of gently north- or south-facing benches and steeper eroded south-facing slopes (Figures 11a and 12a). The benches are 100 m to ~2 km long and ~20–450 m wide. They represent the top surfaces of coherent blocks that have slid downsloped from the top of the wall (Figures 12a and 12c). The intervening south-facing scarps are ~45–~250 m high. They bear decameter-scale erosional ridges and gullies that connect to multiple generations of overlapping debris cones at the base of these scarps (Figure 12a). Several north-facing, E-W to WNW trending antithetic faults offset these erosional ridges and gullies (Figures 12a, 12b, and 12d).

Going upslope from the first outcrop of thick sediments at ~2,603 mbsl (Figure 10e), ROV dive 647 encountered smooth sedimented terrains, sedimented talus (photos no. 31 and 34 in Figure S4 in Supporting Information S1), and a hectometer-sized patch of recent (non-oxide-coated) carbonate-indurated sediments (photo no. 34 in Figure S4 in Supporting Information S1). The first notable scarp, at 2,434 mbsl (location 28 in Figure 11a), exposes a chaotic formation of serpentinite gouge and microbreccia with an irregular foliation (Figure 10f). This outcrop is unconformably covered by about 1 m of semi-consolidated sedimented talus and pelagic sediments. It is free of oxide coating and therefore has been recently rejuvenated. Next, dive 647 explored the head scarp (up to ~55–

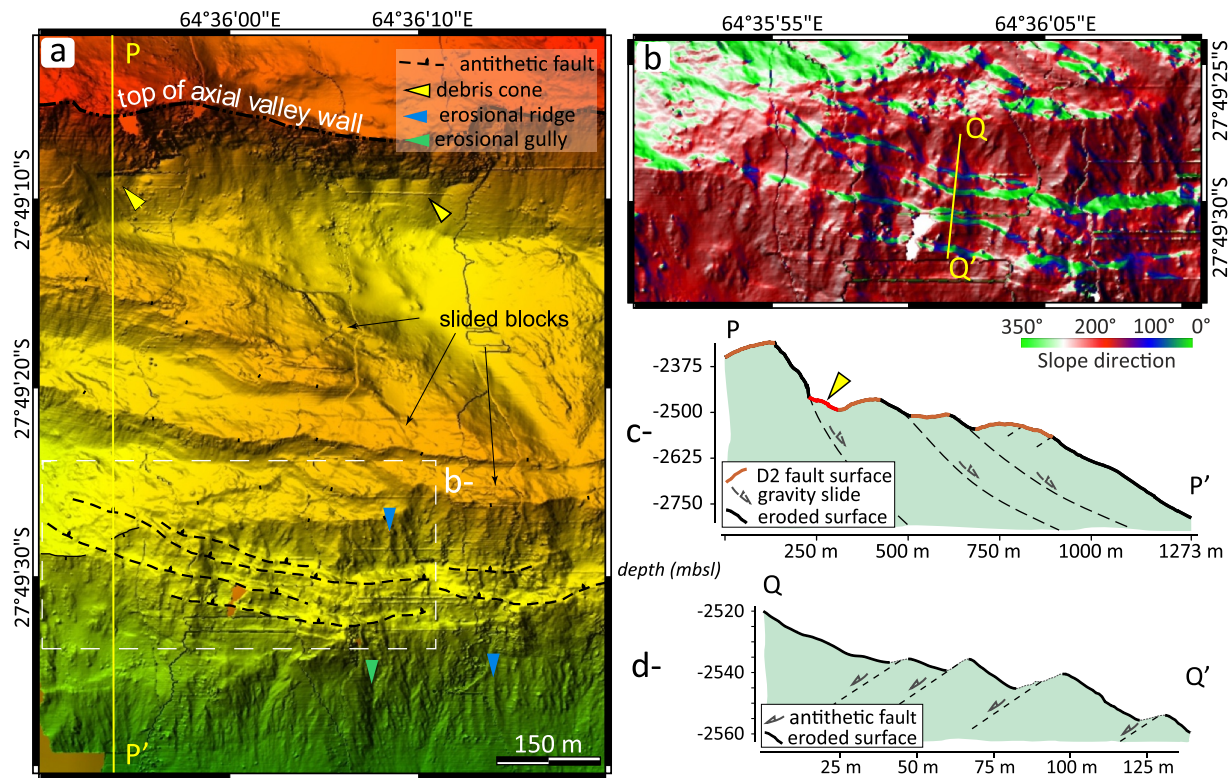


Figure 12. Mass-wasting and antithetic faults in the degraded breakaway (DB) domain. (a) Microbathymetry (map 642, located in Figure 9a, same depth color scale). The edge of hectometer-sized three slid-down blocks is eroded in the form of more recent gullies, erosional ridges, and debris cones. (b) Slope direction map (located in a) showing detail of WNW-trending antithetic normal fault scarps cutting through erosional ridges along the edge of the southernmost slid-down block. (c) Topographic section is located in (a). (d) Topographic section is located in (b).

200 m high) just below the top of the axial valley wall (Figure 11a). At the top (at $\sim 2,315$ mbsl), there is a ~ 1 – 2 m thick, oxide-coated indurated sediment formation (Figure 11b) similar to what is encountered (at $\sim 2,603$ mbsl) earlier at the base of the DB domain (Figure 10e). The edge of the scarp exposes extensively brecciated serpentinites with a thinner oxide-coating, or in several locations, oxide-free with recent talus, indicating the recent mass wasting. These brecciated outcrops display meter to several centimeters-thick pale green, serpentine gouge-bearing horizons (Figure 11d) intercalated with brecciated and locally schistose serpentinite with sigmoidal phacoids (Figure 11c). Pale green gouge-bearing horizons are found at the top of the wall but also deeper down the scarp (the outcrop in Figure 11d is ~ 55 m below the top). The schistosity, the alternation of more and less schistose horizons, and the gouge-bearing horizons all have a moderate dip to the north, sub-parallel to the dominant slope at the top of the wall, indicating that this deformation sequence relates to the D2 detachment fault.

The top of the axial valley wall was also mapped (MAP-639; Figure 1b) and explored further to the west during ROV dive 643. This is a geologically more complex and under-documented region of the wall. There are several volcanic ridges in the axial valley and on the lower slopes of the wall at that longitude (Figure 1b and Sauter et al., 2013). Here, a few gabbroic samples were also collected in addition to serpentinitized peridotites (Figure 1b). Topographically, it is also a complex region: the top of the wall curves southward just west of the area explored during ROV dive 643 (Figure 1b), and the north-facing slopes of the wall are affected by significant mass wasting (Figure S5b in Supporting Information S1). As a result, the top of the axial valley wall is a steep crest (Figure 13a), with slopes locally $>50^\circ$ on the north-facing scarp, that exposes nearly continuous outcrops over a ~ 100 m drop.

ROV exploration dive 643 first briefly explored the northern slopes of the axial valley wall (Figure 13a). These are structured by narrow (≤ 20 m-wide) slope-parallel benches separated by 35 – 40° NW-facing eroded slopes. These eroded slopes expose slope-parallel (i.e., dominantly NW-facing) breccia-lined fault planes (Figure 13b), variably schistose and brecciated serpentinite with sigmoidal fractures (Figure 13c), and occasional decimeter-thick intervals of pale green serpentinite gouge, also dipping to the north-west (photos no. 2 and 4–6 in Figure

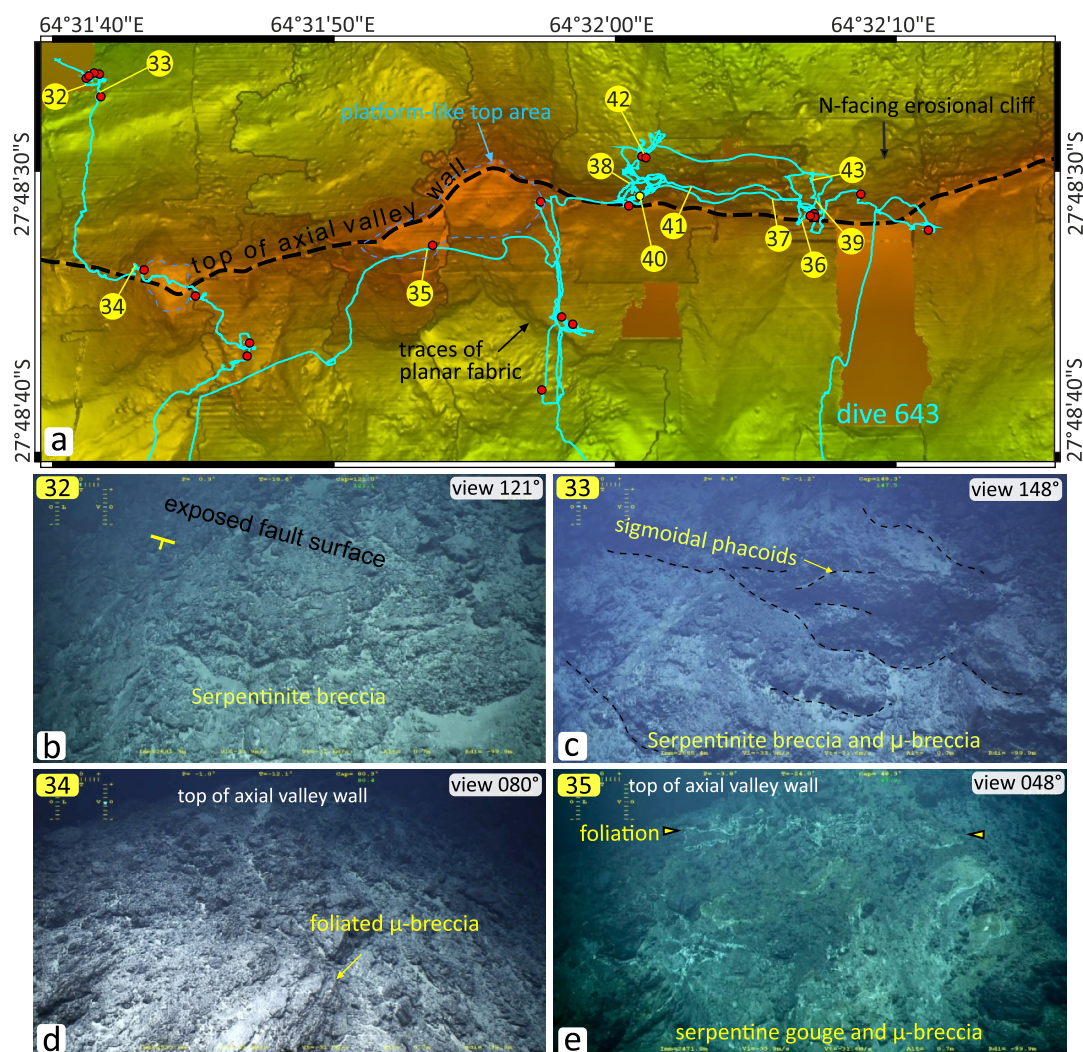


Figure 13. D2 exposed fault surface explored during dive 643 in the west of the study area. (a) Microbathymetry (map 639, located in Figure 2a, same depth color scale) shows the location of rock samples and the track of dive 643. Numbers in yellow circles correspond to the location of seafloor video snapshots shown in panels (b–e; field of view ~15–20 m in foreground) and in Figure 14. Other dive video snapshots from dive 643 are located and shown in Figures S5a and S6 in Supporting Information S1. The top of the axial valley wall in this region is limited by erosional head scarps on both its south and north sides. It, therefore, forms a narrow ridge with steep scarps on both sides. Panels (b) and (c) show brecciated serpentinitized peridotites exposed a bit downslope on the northern flank of the axial valley wall. Panels (d) and (e) show serpentinite gouge and microbreccia with north-dipping (d) or sub-horizontal anastomosing (e) foliation, exposed in platform-like sections of the top of the axial valley wall.

S6 in Supporting Information S1). At the crest-shaped top of the ridge valley wall, the topography is smooth, exposing either brecciated serpentinite with a dominantly north-dipping schistosity with scaly tear-apart structures indicative of normal, top-to-the-north displacement (Figures 13b and 13d) or a chaotic formation of microbreccia with gently dipping horizons of pale green serpentinite gouge intervals (Figure 13e) that hardly emerges from the topography. The shallowest sections of the crest (<2,500 mbsl) expose this microbreccia formation and form small polygonal platforms, dipping <15° to the south or the north (Figure 13a). To the south of one of these platforms, the microbathymetry reveals ~5–20 m high steps that appear to be the trace of an ESE-dipping planar fabric (Figure 13a). ROV dive 643 explored the eroded south-dipping slopes to the east of these steps and documented fractured to schistose and brecciated to massive serpentinites with slope-parallel fractures (photos no. 24, 25, and 27–29 in Figure S6 in Supporting Information S1).

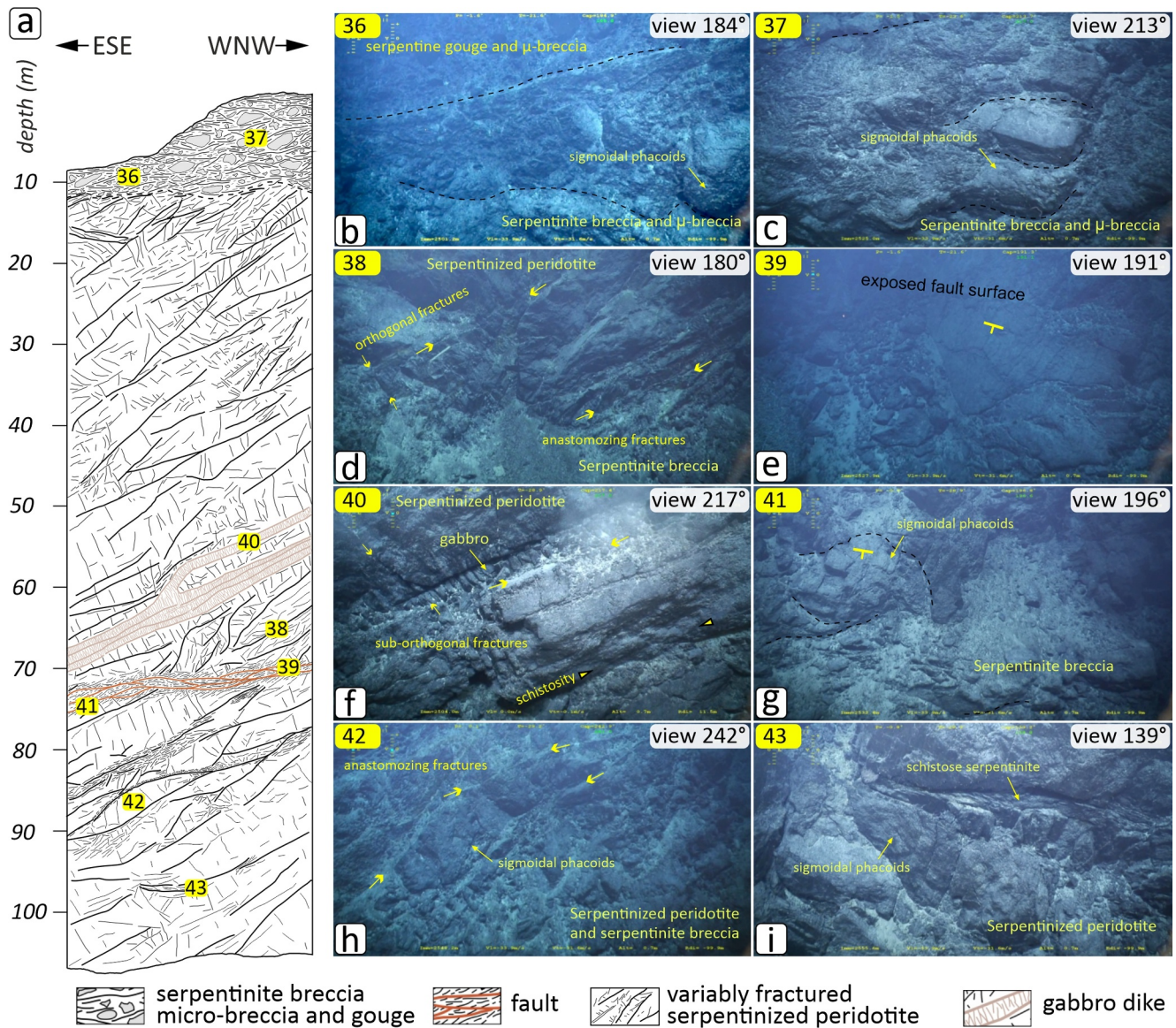


Figure 14. A generalized litho-structural log of the D2 detachment fault zone based on dive 643 observations made along the ~100 m-high north-facing erosional cliff at the top of the axial valley wall (Figure 13a). Numbers in yellow circles in (a) correspond to the seafloor video snapshots shown in panels (b–i); field of view ~15–20 m in foreground) and to locations in Figure 13a. The top of the wall exposes the most deformed facies (serpentinite gouge, microbreccia, and breccia) with gently dipping to horizontal sigmoidal foliations, resting unconformably on variably deformed serpentinitized peridotites. These have ESE-dipping structures, ranging from massive with sets of orthogonal fractures (d and f) to brecciated with sigmoidal fractures and local schistose intervals (d and h). Midway down the cliff, there is an N-dipping exposed fault surface (e). The dominant set of sigmoidal fractures in the brecciated serpentinites below this fault also dips to the north (g).

ROV dive 643 then performed two traverses of the nearly continuous outcrops forming the ~100 m high scarp on the north side of the summit crest (Figure 13a). The outcrop contains a few decimeter-thick gabbro dikes (identified based on sampling and the prominence of sub-orthogonal joints; Figure 14f and photos no. 33–34 in S6). The top ~5–15 m consists of extensively brecciated serpentinites with a gently north-dipping schistosity and local, vein-like pale green serpentine gouge horizons (Figures 14a–14c). Below this brecciated horizon, the dominant fabric consists of sets of fractures similar to those observed in association with D1 fault zone exposures further down the axial valley wall, with a progression from massive outcrops with orthogonal fracture sets (Figure 14f) to brecciated and locally schistose outcrops with anastomosing fractures that define sigmoidal phacoids (Figures 14d, 14h, and 14i). This fabric dips to the ESE and therefore is discordant to the schistosity in the overlying breccia (Figure 14a). It is also discordant to decameter-sized fault planes (Figure 14e) and several meter-thick schistose intervals (Figure 14g) that also dip to the north at several locations within the fractured

sequence. Such discordant relations between the most deformed (fault surfaces, schistose horizons, gouge, and foliated microbreccia) and the less deformed (planar and sigmoidal-shaped fractures) intervals are also very similar to those observed in association with D1 fault zone exposures (Figures 6d and 8b). The outcrop described in Figure 14 extends ~300 m east-west along the slope. The observed ESE-dipping fabric in this area could correspond to the planar fabric observed south of the summit crest ~200 m to the southeast (Figure 13a).

4. Discussion

4.1. Test of the Flip-Flop Hypothesis, Nature of the Degraded Exposed Fault Zone (DEFZ), and the Role of Mass Wasting in Early to Current D1 Exhumation Stages

Dive observations and in situ rock sampling show that the southern slopes of the axial valley wall expose almost only serpentinized peridotite, which confirms that the D1 detachment is nearly amagmatic (Sauter et al., 2013). Our observations also show that north-facing fault surfaces and fault zones with top-to-north displacement are exposed in the degraded breakaway (Figure 10f) and north of the axial valley wall top (Figures 13b and 13c). These outcrops are blanketed by ~1–2 m of semi-consolidated pelagic sediments, with a cm-thick coating of iron-manganese oxides (Figures 10e, 10f, and 11b), indicating a much older seafloor. This is consistent with the interpretation of the 64°35'E SWIR region as dominated by flip-flop (Reston & McDermott, 2011) detachment faulting (Sauter et al., 2013). In this interpretation, the northern slopes of the south-facing axial valley wall expose the older fault surface of the north-facing D2 detachment (Figure 1b).

Our observations also show that the upper slopes of the footwall of the D1 detachment are made of hectometer-to-kilometer-sized blocks of the former breakaway that have slid downslope due to gravity (Figures 2c and 12). Following Cannat et al. (2019), we propose that these large blocks formed early in the development of detachment D1 because, in these initial stages, it emerged with a dip that exceeded the stability of the exhumed serpentinized peridotites (Cannat et al., 2013). Similar degraded breakaways have been documented in MAR corrugated detachments (Escartín et al., 2017; Smith et al., 2014). The deepest exposures of the sedimented D2 fault surface are located ~1.9 km downslope from the top of the wall (Figure 10e). This ground-truthing evidence allows us to confirm the amount of breakaway erosion in the early stages of D1 faulting hypothesized by Cannat et al. (2019) based solely on shipboard bathymetry data. Our observations, therefore, also support the ~300 kyr age estimated for the initiation of D1 by these authors (based on the ~4 km horizontal distance between the emergence and the reconstructed breakaway, assuming a fully tectonic plate divergence).

We also documented outcrops of south-dipping D1 fault surfaces at depths up to 2,653 mbsl in the degraded exposed fault zone (DEFZ) domain. However, this domain has a chaotic topography distinct from the more regular slopes in the exposed fault zone (EFZ) domain below. Our interpretation, sketched in Figures 2c and 15a, is that, in the DEFZ domain, the D1 fault zone dissected previously slid-down blocks (and their basal surfaces) of the degraded breakaway. Similar interactions between mass-wasting and normal faulting in the early stages of a detachment's activity have been documented at the MAR 13°30'N ODF (Escartín et al., 2017) and were tentatively proposed for the D1 detachment in Figure A1 of Cannat et al. (2019).

The lobate morphologies visible at the bottom of the D1 footwall (Figure 2a) may be interpreted as toes of more recent debris flows, burying the D1 fault emergence. However, our dive observations indicate that this is not the case, at least in the investigated 64°36'E region: ROV dive 649 documents exposures of south-dipping D1 fault surfaces along the lobate base of the axial valley wall (Figures 3a and 6a) and along the NNE trending western limit of this lobe (Figure 6a). This indicates that this lobe is defined by the local D1 emergence geometry. While we cannot exclude that other lobes identified in Figure 2a might be composed of debris, we thus conclude that there is, at this point, no conclusive evidence for large-scale recent mass-wasting forming the toe of the axial valley wall.

4.2. Corrugated Versus Smooth Seafloor

Below the DEFZ domain and down to the base of the D1 footwall, ROV dives document frequent outcrops of fault surfaces and deformed serpentinized peridotites. Most of this terrane consists of in situ D1 fault zone material with talus (Figures 3b, 3c, and 6a) and erosional scarps (Figure 6a). In the west, this exposed fault zone (EFZ) is structured by prominent NNE-trending ridges (A, B, and C in Figure 2a), which we interpret as large (up to ~150–300 m in amplitude and ~0.7–2 km in wavelength) members of the corrugation family (i.e., undulations of the

fault surface itself). Our key supporting observation is that, as we ascend ridge A along dive 644 (Figure 3a), fault surfaces and underlying dominant structures (e.g., fractures) consistently dip southwest, south, or southeast, mirroring the local slope (Figure 8).

Smaller, hectometer-spaced undulations (up to ~45 m in amplitude) that unambiguously belong to the family of ODF corrugations (Cann et al., 1997; Escartín et al., 2017; MacLeod et al., 2009; Smith et al., 2006) are also visible in the microbathymetry map of ridge B (Figures 3b and 3c). Some of these features can be followed for at least 350 m across the microbathymetry coverage, but they are not visible in the shipboard bathymetry because they are obscured by the complex ridge and gully shaped topography of the area (Figure 3a).

Dive observations also show numerous outcrop-scale undulations (amplitude <1 m), which we relate to the decameter-sized anastomosing fabric of the exposed fault (Figures 6c, 6g, 6h, and 8f) and to fainter lineaments visible in the microbathymetry (Figures 3b and 6a). Such variability in the amplitude of ODF corrugations, from meter to hectometer and even kilometer scales, is consistent with observations at several domal and corrugated exposed ODF surfaces (Cann et al., 1997; Escartín et al., 2017; Searle et al., 2003; Smith et al., 2014; Tucholke et al., 1998). This variability and a compilation of outcrop-scale observations led Escartín et al. (2017) and Parnell-Turner et al. (2018) to suggest that while ODF corrugations vary in scale, they share a common mechanism of formation, resulting from several scales of heterogeneous strain localization in anastomosing fault networks. Our observations of hectometer- and decameter-spaced corrugations in the D1 footwall are consistent with this interpretation. We extend this interpretation to the kilometer-scale undulations forming the NNE-trending ridges, suggesting that these undulations could correspond to the shape of fault splays surrounding elongated km-scale (mega) phacoids (Figure 15a).

To the east of NNE-trending ridge C (Figures 2a and 15a), the EFZ domain is smooth with lobate scale-like structures best seen in TOBI images (Figure 2d). NNE-trending ridges are absent, and the sparse microbathymetry coverage shows no corrugations (Figure 6a). There, ROV dives document thick horizons (up to ~8 m thick; Figure 4a) of gouge-bearing brecciated serpentinites, with microstructures that suggest a mix of brittle and semi-brittle deformation mechanisms (Figures 4d–4g). Dive observations also suggest that the gouge and microbreccia intervals originate in fractures in more coherent serpentinitized peridotite intervals (Figure 5a). We propose that these fractures create pathways for hydrous fluids, favoring the recrystallization of serpentinite in gouge intervals, leading to strain localization and further semi-brittle deformation and fault weakening. Fractures cutting into moderately deformed mega-phacoid cores could, by this mechanism, turn into weak gouge-bearing shear zones and subdivide initially elongated and thicker phacoids into less elongated ones (Figure 15c), preventing the formation of corrugations at kilometers to several hectometer scales and instead creating the flat scale-like lobate and arcuate tear-apart structures observed in the TOBI image (Figure 2d). A key observation in support of this interpretation is the angular discordance observed in both D1 (Figures 6d and 8b) and D2 (Figures 14a and 14b) fault zones between the anastomosing fabric of serpentinitized peridotite outcrops and the schistosity/foliation in microbreccia and gouge horizons (Figure 15e). This indicates that gouge-bearing shear zones cut into pre-existing phacoids and brittle fault splays.

4.3. The D1 Damage Zone at Depth

As mentioned before (Section 4.1), we initially envisioned that lobate slope break structures at the base of the D1 footwall (Figure 2a) could be kilometer-wide debris lobes. While this might be the case outside our investigated area, microbathymetry and ROV observations made along dives 644 and 649 (Figures 2a, 3a, and 6a) support an alternative interpretation in which the lobes, indentations, and NNE-trending ridges form due to the activation of fault splays surrounding hectometer to kilometer-sized mega-phacoids within a broad D1 fault zone (Figure 15a). The (north-south) indentation of D1 emergence near the tip of ridge C is ~1.2 km long (Figure 3a). We propose that it formed because most, if not all, of the displacement was transferred from a fault splay that emerged further down near the base of the axial valley wall to a more internal fault splay that is currently active (Figure 3a). The maximum dip of exposed fault surfaces was documented near the emergence and at the two farthest points in the indented region (Figures 3a and 6a). Taking a 30° average dip angle for the two proposed fault splays, the observed 1.2-km distance translates to an across-fault splay perpendicular distance (i.e., mega-phacoid thickness) of ~600 m. Thus, we propose that the D1 damage zone is at least that broad and comprises anastomosing domains of more localized deformation (i.e., fault splays/strands) that can change activation status through time (Figure 15a). The mega-phacoid geometries are also reflected by the undulation amplitudes (e.g., half mega-

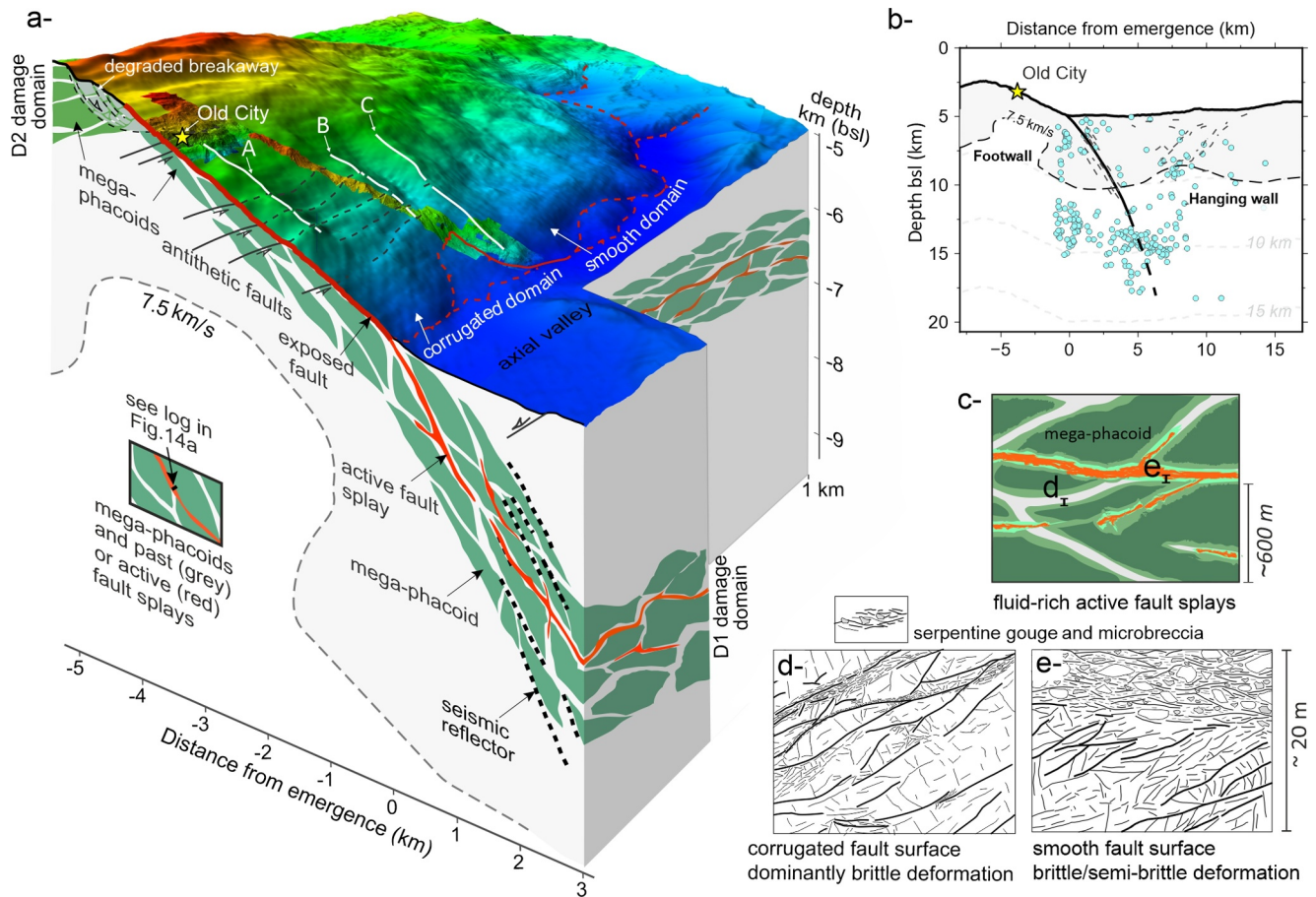


Figure 15. Possible anatomy of the D1 footwall and damage zone, extending down to ~ 9 km below its emergence. The conceptual sketch in (a) is constrained by the synthetic sketch in (b), which shows the distribution of earthquakes recorded in the $64^{\circ}30'E$ Southwest Indian Ridge (SWIR) region during two 2–3-week periods in 2014 and 2016 (Chen et al., 2023). Additionally, it incorporates the 7.5 km/s V_p isovelocity contour from Corbalán et al. (2021) and the trace of seismic reflectors from Momoh et al. (2017). The 3D conceptual sketch in (a) is drawn from our seafloor topography and geological findings. The width of the damage zone (~ 1 – 1.8 km) for both D1 and D2 is inferred from the distribution of seismic reflectors along D1. The size of megaphacoids (which are domains of moderately fractured serpentinized peridotite) is inferred from hectometer to kilometer-sized D1 footwall undulations, lobate structures and indentations at the D1 emergence. The conceptual sketch in (c) focuses on the D1 fault zone, located ~ 1 km south of its emergence, highlighting the geometry of anastomosing highest strain localized horizons and fluid-poor dominantly brittle deformation in (d) as well as fluid-enhanced semi-brittle deformation in (e), both of which are shown in (c). Panels (d) and (e) are outcrop-scale sketches of active/inactive fault splay based on dive observations. Further explanations can be found in the text.

phacoid thickness; up to ~ 150 – 300 m) and wavelengths (up to ~ 0.7 – 2 km) of the exhumed NNE trending ridges. Lobes and indentations are also common along the D1 emergence in the eastern smooth domain (Figure 2a), suggesting that mega-phacoids are also present in the damage zone there, although probably flattened and subdivided by gouge-bearing shear zones (Figures 15a, 15c, and 15e). The broad anastomosing fault zone structure proposed in Figure 15a is consistent with observations and geophysical data from other complex plate-bounding fault systems, such as the Alpine Fault Zone in New Zealand (Lay et al., 2016; Lukács et al., 2018; Schuck et al., 2020) and the San Andreas Fault system (Fletcher et al., 2020). Distinct fault splays within the San Andreas Fault system have been shown to be seismically active simultaneously (Dor et al., 2006; Sieh, 1978).

Fault splays, both active and formerly active, between the mega-phacoids are estimated to be ~ 200 m-thick, based on the lithostructural log shown in Figure 14a. This assumes that the most intensely strained regions, which may eventually form the exhumed fault surface, are centered relative to adjacent mega-phacoids (Figure 15c). Arrays of subparallel seismic reflectors interpreted as zones of fault damage by Momoh et al. (2017) dip $\sim 50^{\circ}$ at 5 km depth (below the axial valley floor) and are distributed over ~ 1.8 km (Figures 15a and 15b). We take this as the across-fault width of the D1 damage zone at those depths and draw the same mega-phacoids configuration for the D2 damage domain (Figure 15a). We also drew a thinner damage zone up in the DEFZ and upper EFZ regions of the D1 footwall because they exposed younger portions of the D1 fault, which had accumulated less displacement.

Based on dive observations, we also draw the exposed D1 fault surface in the DEFZ domain as cutting through slid-down blocks of the degraded breakaway (Figure 15a).

The estimated thickness of fault zones exposed by D1 and D2 detachments (~100 m; Figure 14a) is comparable to that documented at the Atlantis Massif (Karson et al., 2006), 15°45'N (MacLeod et al., 2002) and 13°20'N (Escartín et al., 2017; Parnell-Turner et al., 2018) dome-shaped corrugated ODFs in the MAR. The fault zone at the 13°20'N ODF is described as ~75 m thick, with individual fault rock exposures, mostly in basalts, show brittle deformation structures comparable to those documented in the least deformed portions of the detachment fault zone shown in Figure 14a. Also, while kilometer-sized phacoids have not been documented in dome-shaped ODFs, and earthquakes within these ODFs tend to align along the detachment fault trace at depth (deMartin et al., 2007; Parnell-Turner et al., 2017). This contrasts with the seismicity pattern recorded at the D1 SWIR detachment, with earthquakes scattered into both the hanging wall and the footwall (Figure 15b; Chen et al., 2023). Also, the scarce seismic reflection data available for dome-shaped ODFs (Canales et al., 2017; Jian et al., 2024) do not show stacked fault zone reflectors like those imaged beneath the emergence of D1 (Figures 15a and 15b; Momoh et al., 2017). Although none of these observations is conclusive, together they suggest significant differences in the fault damage zone thickness and mechanical behavior between the two settings, with flip-flop ODFs exhibiting more distributed deformation and thicker damage.

Deformed assemblages are also different. While isolated samples of cataclastic and semi-brittle gouges have been reported at more magmatic dome-shaped corrugated ODFs (Bonnemains et al., 2017; Picazo et al., 2013; Schroeder & John, 2004; Schroeder et al., 2007), these ODFs lack exposures of meter-thick serpentinite gouge-bearing horizons. Instead, these dome-shaped corrugated ODFs expose talc, amphibole, and/or chlorite-bearing serpentinite schists (Boschi et al., 2006; Dick et al., 2002; Escartín et al., 2003; Hansen et al., 2013; Picazo et al., 2012; Schroeder & John, 2004), which are uncommon at SWIR flip-flop detachments (Bickert et al., 2023). Amphibole-bearing assemblages are stable at temperatures higher than the retrograde stability limit of serpentinite minerals (~450°C; e.g., Früh-Green et al., 2004). They may thus play a role in localizing detachment-related deformation in the lower brittle lithosphere (e.g., Picazo et al., 2012). Therefore, while serpentinite microbreccia and gouges make for weak fault splays in the upper brittle lithosphere of flip-flop detachments, uncommon amphibole-bearing schists would make for a stronger lower brittle lithosphere, with less efficient strain localization than at domal ODFs (Bickert et al., 2023). Furthermore, lacking the weak magma-infiltrated regions that probably characterize the base of the axial lithosphere at domal ODFs (e.g., Casini et al., 2021; Olive et al., 2010; Picazo et al., 2012), the flip-flop detachment settings also have a strong, ductile lithosphere with distributed high-stress semi-brittle deformation (Bickert et al., 2020, 2021). Based on these observations, we propose that the broad damage zone documented here in the serpentine stability field (Figure 15a) is at least partly inherited from distributed detachment-related fault zones deeper in the axial lithosphere.

4.4. Are Antithetic Minor Normal Faults in D1 Footwall Incipient Flip-Flop Faults?

We document several antithetic, WNW-trending, and north-facing normal faults with meter to decameter-scale offsets that extend up to ~4.5 km along-axis in the western corrugated domain of the footwall (Figure 15a). These faults occur from the base of the EFZ domain up the wall into the DB domain (Figures 12b and 15a). They dissect recent talus and erosional ridges and are therefore very recent and probably active (Figures 3c and 12b). Such antithetic faults do not occur in the non-corrugated eastern part of the study area (Figures 2a and 15a). Together, antithetic faults numbered #1 to 10 in Figures 3a and 9a have an estimated cumulated horizontal offset of ~285 m (estimate made for an average 35° dip based on the exposed fault plane in Figure 7b).

Small-offset normal faults deforming the exhumed footwall have been reported in continental detachment fault systems (Little et al., 2019; Mizera et al., 2019) and at corrugated domal ODFs on the mid-Atlantic ridge (Atlantis Massif; Karson et al., 2006, and 13°40'N; Escartín et al., 2017). The distribution of microseismicity also suggests their presence in the TAG (Trans-Atlantic Geotraverse) detachment footwall (deMartin et al., 2007).

Numerical simulations of ODF formation provide several perspectives to interpret such antithetic normal faults. Kinematic models involving flexural deformation of the ODF footwall in response to unloading stresses caused by detachment faulting predict extension in the shallow footwall and compression in the lower half of the plate (Buck, 1988). In the models of Sandiford et al. (2021), the ODF footwall undergoes a solid block rotation controlled by the concave downward shape of the detachment. Within this framework, normal faulting in the footwall accommodates the flexure required to transition from solid block rotation along the detachment to horizontal plate

divergence after exhumation. Thermo-mechanical models of amagmatic spreading of a thick axial lithosphere, designed to study the SWIR 64°E flip-flop detachment setting (Bickert et al., 2020; Demont et al., 2024; Glink & Hasenclever, 2024; Mezri et al., 2024) or the Flemish Cap-Galicia conjugate margins (Theunissen & Huisman, 2022) offer additional insights. In these simulations, incipient antithetic normal faults that form in the footwall of active detachments can evolve differently depending on subtle variations in simulation parameters. In some cases, they evolve into a conjugate to the main fault (the “horst-mode” of Bickert et al., 2020) and then take over as a new antithetic detachment (the “flip-flop mode”). In other cases, the antithetic fault dies off as displacement along the main fault continues (Demont et al., 2024). Whatever the case, in these simulations, antithetic faults typically do not form in the very early stages of a detachment’s lifespan. They are focused on a single fault zone and not distributed over the entire height of the footwall, as documented in our observations (Figure 15a). However, these numerical models, with grid spacing ≥ 500 m, do not have the resolution to produce such distributed and small offset faults. Our preferred interpretation is that the antithetic normal faults documented in this natural case represent early stages (given their small cumulated displacement and the young age of D1) of delocalized antithetic brittle failure in the D1 footwall. Based on measured breakaway to emergence horizontal distances in the 64°35′E SWIR flip-flop detachment system, which range from 9 to 21 km (Cannat et al., 2019), it is unlikely that these small antithetic faults will evolve into a full-fledged new flip-flop detachment in the future.

4.5. Along-Axis Variations of the Strength of Young Flip-Flop Detachments Footwalls

Due to the lesser abundance of serpentinite gouge and microbreccia, the overall rheology of the fault zone in the corrugated western domain of the D1 footwall (Figure 15a) is closer to purely brittle (Figure 15d) and probably stronger than in the eastern smooth domain (Figure 15e). This difference in fault strength probably also applies to the D1 footwall. A stronger footwall in the west is consistent with higher bending forces, a higher footwall relief, and the development of antithetic normal faults (Figures 2a and 15a). D2 fault zone exposures show thick intervals of gouge and microbreccia (Figures 11c, 11d, and 13e), suggesting that the non-corrugated, gouge-rich, and weaker D1 fault zone configuration in the east is common at mature flip-flop detachments (D2 fault zone exposures at the top of D1 footwall are estimated to have formed after ~ 17 km of displacement on D2; Cannat et al., 2019). If the abundance of serpentinite gouges does, as we propose, reflect the availability of hydrous fluids during deformation, it makes sense that it should increase from the early stages of a detachment activity as deformation creates more pathways for seawater-derived fluids into and around the damage zone. Our proposed interpretation is, therefore, that the along-axis contrast between the smooth, non-corrugated eastern domain and the probably stronger footwall to the west results from lateral variations in the permeability of the young D1 fault and footwall. These variations might become more subdued later in D1 lifespan as the weaker, serpentinite gouge-rich rheology becomes more prevalent. Of course, it is possible that initial permeability variations in the young D1 footwall were at least partly inherited from heterogeneities in the footwall of the previous, more mature, and antithetic D2 detachment.

The 2D velocity model of Corbalán et al. (2021), at the longitude of dive 644 (Figure 1b), shows an updip shallowing of the 7.5 km/s isovelocity contour ($\sim 15\%$ serpentinization; Miller & Christensen, 1997), suggesting relatively low hydration of the exhumed mantle in the footwall of D1 at the longitude of the corrugated domain (Figures 15a and 15b). Unfortunately, no equivalent seismic profile is available to test whether the D1 footwall is more thoroughly hydrated in the eastern, smooth domain. A recent 3D seismic study (Robinson et al., 2024) covers the axial valley floor south of the emergence of D1 and extends to the south beyond the breakaway of detachment D2 (Figure 1a). It identifies lateral along and across-axis variations in P wave seismic velocity (V_p) over distances of ~ 20 km and down to 3.4 km below the seafloor. These V_p anomalies are consistent with lateral variations in the degree of hydration (serpentinization) in the upper lithosphere formed at flip-flop detachments (Robinson et al., 2024) but do not document the V_p structure of the D1 footwall.

The corrugated and presumably stronger western D1 footwall domain in Figure 15a is also where the relief of the axial valley wall is the highest ($\sim 2,750$ m). It is less high further to the east ($\sim 2,250$ m at longitude 64°41′E, ~ 8 km to the east; Figure 1b). The D1 footwall is therefore a 3D deformation structure imposed on the D2 exhumed fault surface and basement. The formation of this relief back tilted the exhumed D2 fault surface by as much as 15° in our study area and may have enhanced the curvature of the E2 emergence trace, which curves around the most elevated D1 footwall region (Figure 1a). Looking at the undulations of past detachments’ emergence traces in Figure 1a, we note that they too, tend to curve around the most elevated regions of the next detachment’s breakaway (e.g., emergence E3 and breakaway B2 in Figure 1a). 3D deformation of the D1 footwall

could also have induced smaller scale deformation of the former D2 seafloor, forming the NW/NNW-trending, ~0.6–1.5 km long and up to ~100 m high undulations of the seafloor visible in the north flank of the D1 footwall at the longitude of dive 649 (Figures 1b and 2a). However, this remains to be tested with geological observations.

Three-dimensional internal deformation of the D1 footwall could also explain why the dominant trend of hectometer and decameter-spaced corrugations documented in this study, and of the NNE-trending ridges (A-C), which we interpret as mega-corrugations, is N25° (Figure 3). This orientation is at a slight clockwise angle to the N355–N10° recent spreading direction in this region of the SWIR (Cannat et al., 2006; Lemaux et al., 2002; Patriat & Segoufin, 1988). Corrugations reported at dome-shaped detachment fault surfaces at the MAR and SWIR are mostly parallel to the spreading direction (Cann et al., 1997; Cannat et al., 2009; MacLeod et al., 2009; Smith et al., 2006). We tentatively propose that the small angular discordance between corrugations and the spreading direction in our study area is due to a local clockwise strain rotation in the deforming D1 footwall. This interpretation, and more generally, understanding the origin and consequences of along-axis strength variations in young flip-flop detachment footwalls, requires further testing with new microbathymetry data and additional dive observations.

5. Conclusions

Using shipboard bathymetry, microbathymetry, remotely operated vehicle (ROV) dive observations, and in situ rock samples, we constrain the anatomy and deformation of two successive “flip-flop” detachment fault zones exposed in the northern axial valley wall of the Southwest Indian Ridge (SWIR) at 64°35′E. Our findings and preferred interpretations are:

1. The south-facing axial valley wall exposes variably deformed serpentized peridotites, including serpentinites, microbreccia, gouge, and rare gabbro dikes. The top of the wall exposes sections through the older D2 detachment fault zone. The southern slopes expose 3 structural domains related to the presently active D1 detachment: the degraded breakaway (DB) with slid-down blocks of the initial breakaway, formed by mass-wasting in the earliest stages of D1 activity, ~300 kyrs-ago; the degraded exposed fault zone (DEFZ), a narrow intermediate domain in which a still very young D1 cut through slid-down material; and the exposed fault zone (EFZ) that extends down to the bottom of the wall and exposes outcrops of variably deformed and locally corrugated D1 fault zone material.
2. The D1 detachment fault zone and footwall show significant three-dimensional and non-planar variations in structure and morphology. ROV dives document a western domain that locally exposes corrugated fault surfaces, NNE-trending km-scale ridges that we interpret as mega-corrugations, and sets of very recent minor antithetic normal faults that we interpret as due to footwall bending stresses. To the east, the EFZ domain has a smoother topography, lacks corrugations, mega-corrugations, and antithetic faults, and exposes thicker outcrops of serpentinite microbreccia and gouges (up to ~8 m thick). We propose that these differences result from a contrast in fault and footwall rheology, with a stronger corrugated domain to the west and a weaker smooth domain to the east. We further propose that this contrast is related to lateral variations in the availability of hydrous fluids during deformation in the young D1 detachment, with higher fluid availability resulting in thicker and more pervasive horizons of weak serpentine gouges. This contrast can be expected to be highest in the early stages of a new detachment, as brittle deformations open new pathways for seawater-derived fluids into the young fault zone and footwall.
3. ROV dives show that the emergence trace of D1 near the base of the axial valley wall is not rectilinear but lobate, with indentations that we interpret as fault splays linking hectometer-sized mega-phacoids of less deformed serpentized peridotites. We estimate the minimum thickness of the emerging D1 damage zone to be about 600 m. While individual fault splays are similar in thickness (~100 m) to those documented at ODFs in more magmatic settings, the overall detachment damage zone is therefore probably thicker. We propose that this thick damage zone is, in part, inherited from the less localized semi-brittle deformation documented by Bickert et al. (2021) in the root zone of nearly amagmatic SWIR flip-flop detachments.

Data Availability Statement

Medium-resolution versions of the ROV dive videos, raw microbathymetry data, and other data acquired during the ROVSMOOTH cruise are accessible at <https://doi.org/10.17600/16002000>. Processed microbathymetry grids

are available in open access on the SEANOE data service (<https://doi.org/10.17882/103743>). This article forms part of S.M.'s doctoral thesis. S.M. analyzed and interpreted the data and wrote the draft of the manuscript. M.C. developed the project, led the ROVSMOOTH cruise, and supervised interpretation and writing.

Acknowledgments

We thank Jacqueline Dixon and Vasiliki Mouslopoulou for their editorial handling of the manuscript and two anonymous reviewers for their insightful comments and suggestions. We extend our gratitude to the ROVSMOOTH cruise science parties and the crew of the RV *Pourquoi pas?*. This work was fully supported by the ANR project Ridge-Factory-Slow (ANR-18-CE01-0002). We thank Jean-Arthur Olive and Antoine Demont for several good discussions, Barbara E. John and Daniel Sauter for their advice on an earlier version of the manuscript, and S. Borenszajn for technical assistance at the IPGP SEM facility, supported by the IPGP multidisciplinary program PARI. Open access publishing facilitated by Université Paris Cité as part of the Wiley-Université Paris Cité agreement. This is the IPGP contribution number 4291.

References

- Bickert, M., Cannat, M., & Brunelli, D. (2023). Hydrous fluids down to the semi-brittle root zone of detachment faults in nearly amagmatic ultraslow spreading ridges. *Lithos*, 442, 107084. <https://doi.org/10.1016/j.lithos.2023.107084>
- Bickert, M., Cannat, M., Tommasi, A., Jammes, S., & Lavier, L. (2021). Strain localization in the root of detachment faults at a melt-starved mid-ocean ridge: A microstructural study of Abyssal Peridotites from the Southwest Indian Ridge. *Geochemistry, Geophysics, Geosystems*, 22(5), e2020GC009434. <https://doi.org/10.1029/2020GC009434>
- Bickert, M., Lavier, L., & Cannat, M. (2020). How do detachment faults form at ultraslow mid-ocean ridges in a thick axial lithosphere? *Earth and Planetary Science Letters*, 533, 116048. <https://doi.org/10.1016/j.epsl.2019.116048>
- Bonnemains, D., Escartin, J., Mével, C., Andreani, M., & Verlaquet, A. (2017). Pervasive silicification and hanging wall overplating along the 13° 20'N oceanic detachment fault (Mid-Atlantic Ridge). *Geochemistry, Geophysics, Geosystems*, 18(6), 2028–2053. <https://doi.org/10.1002/2017GC006846>
- Boschi, C., Früh-Green, G. L., Delacour, A., Karson, J. A., & Kelley, D. S. (2006). Mass transfer and fluid flow during detachment faulting and development of an oceanic core complex, Atlantis Massif (MAR 30°N). *Geochemistry, Geophysics, Geosystems*, 7(1), Q01004. <https://doi.org/10.1029/2005GC001074>
- Buck, W. R. (1988). Flexural rotation of normal faults. *Tectonics*, 7(5), 959–973. <https://doi.org/10.1029/TC007i005p0959>
- Buck, W. R., Lavier, L. L., & Poliakov, A. N. (2005). Modes of faulting at mid-ocean ridges. *Nature*, 434(7034), 719–723. <https://doi.org/10.1038/nature03358>
- Canales, J. P., Dunn, R. A., Arai, R., & Sohn, R. A. (2017). Seismic imaging of magma sills beneath an ultramafic-hosted hydrothermal system. *Geology*, 45(5), 451–454. <https://doi.org/10.1130/G38795.1>
- Cann, J. R., Blackman, D. K., Smith, D. K., McAllister, E., Janssen, B., Mello, S., et al. (1997). Corrugated slip surfaces formed at ridge–transform intersections on the Mid-Atlantic Ridge. *Nature*, 385(6614), 329–332. <https://doi.org/10.1038/385329a0>
- Cannat, M., Lagabrielle, Y., Bougault, H., Casey, J., de Coutures, N., Dmitriev, L., & Fouquet, Y. (1997). Ultramafic and gabbroic exposures at the Mid-Atlantic Ridge: Geological mapping in the 15°N region. *Tectonophysics*, 279(1–4), 193–213. [https://doi.org/10.1016/S0040-1951\(97\)00113-3](https://doi.org/10.1016/S0040-1951(97)00113-3)
- Cannat, M., Mahato, S., Martinez, I., Früh-Green, G., Bernasconi, S., Lecoeuvre, A., et al. (2021). Carbonate-Brucite Chimneys at the Southwest Indian Ridge: The Old City hydrothermal field. In *AGU Fall Meeting Abstracts* (Vol. 2021, p. V33A-09). Retrieved from <https://ui.adsabs.harvard.edu/abs/2021AGUFM.V33A..09C/abstract>
- Cannat, M., Mangeny, A., Ondréas, H., Fouquet, Y., & Normand, A. (2013). High-resolution bathymetry reveals contrasting landslide activity shaping the walls of the Mid-Atlantic Ridge axial valley. *Geochemistry, Geophysics, Geosystems*, 14(4), 996–1011. <https://doi.org/10.1002/ggge.20056>
- Cannat, M., Mevel, C., Maia, M., Deplus, C., Durand, C., Gente, P., et al. (1995). Thin crust, ultramafic exposures, and rugged faulting patterns at the Mid-Atlantic Ridge (22–24°N). *Geology*, 23(1), 49–52. [https://doi.org/10.1130/0091-7613\(1995\)023%3C0049:TCUEAR%3E2.3.CO;2](https://doi.org/10.1130/0091-7613(1995)023%3C0049:TCUEAR%3E2.3.CO;2)
- Cannat, M., Rommevaux-Jestin, C., Sauter, D., Deplus, C., & Mendel, V. (1999). Formation of the axial relief at the very slow spreading Southwest Indian Ridge (49 to 69°E). *Journal of Geophysical Research*, 104(B10), 22825–22843. [https://doi.org/10.1016/S0040-1951\(97\)00113-3](https://doi.org/10.1016/S0040-1951(97)00113-3)
- Cannat, M., Sauter, D., Bezos, A., Meyzen, C., Humler, E., & Le Rigoleur, M. (2008). Spreading rate, spreading obliquity, and melt supply at the ultraslow spreading Southwest Indian Ridge. *Geochemistry, Geophysics, Geosystems*, 9(4), Q04002. <https://doi.org/10.1029/2007GC001676>
- Cannat, M., Sauter, D., Escartin, J., Lavier, L., & Picazo, S. (2009). Oceanic corrugated surfaces and the strength of the axial lithosphere at slow spreading ridges. *Earth and Planetary Science Letters*, 288(1–2), 174–183. <https://doi.org/10.1016/j.epsl.2009.09.020>
- Cannat, M., Sauter, D., Lavier, L., Bickert, M., Momoh, E., & Leroy, S. (2019). On spreading modes and magma supply at slow and ultraslow mid-ocean ridges. *Earth and Planetary Science Letters*, 519, 223–233. <https://doi.org/10.1016/j.epsl.2019.05.012>
- Cannat, M., Sauter, D., Mendel, V., Ruellan, E., Okino, K., Escartin, J., et al. (2006). Modes of seafloor generation at a melt-poor ultraslow-spreading ridge. *Geology*, 34(7), 605–608. <https://doi.org/10.1130/G22486.1>
- Casey, J. F. (1997). Comparison of major- and trace-element geochemistry of abyssal peridotites and mafic plutonic rocks with basalts from the MARK region of the Mid-Atlantic Ridge. In J. A. Karson, M. Cannat, D. J. Miller, & D. Elthon (Eds.), *Proceedings of the Ocean Drilling Program* (Vol. 153, pp. 181–241). Scientific Results. <https://doi.org/10.2973/odp.proc.sr.153.012.1997>
- Casini, L., Maino, M., Sanfilippo, A., Ildefonse, B., & Dick, H. J. (2021). High-temperature strain localization and the nucleation of oceanic core complexes (16.5°N, Mid-Atlantic Ridge). *Journal of Geophysical Research: Solid Earth*, 126(9), e2021JB022215. <https://doi.org/10.1029/2021JB022215>
- Chen, J., Crawford, W. C., & Cannat, M. (2023). Microseismicity and lithosphere thickness at a nearly-amagmatic oceanic detachment fault system. *Nature Communications*, 14(1), 430. <https://doi.org/10.1038/s41467-023-36169-w>
- Corbalán, A., Nedimović, M. R., Loudon, K. E., Cannat, M., Grevemeyer, I., Watremez, L., & Leroy, S. (2021). Seismic velocity structure along and across the ultraslow-spreading Southwest Indian ridge at 64°30'E showcases flipping detachment faults. *Journal of Geophysical Research: Solid Earth*, 126(10), e2021JB022177. <https://doi.org/10.1029/2021JB022177>
- deMartin, B. J., Sohn, R. A., Canales, J. P., & Humphris, S. E. (2007). Kinematics and geometry of active detachment faulting beneath the Trans-Atlantic Geotraverse (TAG) hydrothermal field on the Mid-Atlantic Ridge. *Geology*, 35(8), 711–714. <https://doi.org/10.1130/G23718A.1>
- Demont, A., Cannat, M., & Olive, J.-A. (2024). Modes of detachment faulting at slow and ultraslow mid-oceanic ridges. In *EGU General Assembly 2024, Vienna, Austria, 14–19 Apr 2024* (pp. EGU24–15593). <https://doi.org/10.5194/egusphere-egu24-15593>
- Dick, H. J., Natland, J. H., Alt, J. C., Bach, W., Bideau, D., Gee, J. S., et al. (2000). A long in situ section of the lower ocean crust: Results of ODP Leg 176 drilling at the Southwest Indian Ridge. *Earth and Planetary Science Letters*, 179(1), 31–51. [https://doi.org/10.1016/S0012-821X\(00\)00102-3](https://doi.org/10.1016/S0012-821X(00)00102-3)
- Dick, H. J., Tivey, M. A., & Tucholke, B. E. (2008). Plutonic foundation of a slow-spreading ridge segment: Oceanic core complex at Kane Megamullion, 23°30'N, 45°20'W. *Geochemistry, Geophysics, Geosystems*, 9(5), Q05014. <https://doi.org/10.1029/2007GC001645>
- Dick, H. J. B., Ozawa, K., Meyer, P. S., Niu, Y., Robinson, P. T., Constantin, M., et al. (2002). Primary silicate mineral chemistry of a 1.5-km section of very slow spreading lower ocean crust: ODP Hole 735B, Southwest Indian Ridge. In J. H. Natland, H. J. B. Dick, D. J. Miller, & R. P.

- Von Herzen (Eds.), *Proceedings of the Ocean Drilling Program* (Vol. 176, pp. 1–61). Scientific Results. <https://doi.org/10.2973/odp.proc.sr.176.001.2002>
- Dor, O., Rockwell, T. K., & Ben-Zion, Y. (2006). Geological observations of damage asymmetry in the structure of the San Jacinto, San Andreas and Punchbowl faults in Southern California: A possible indicator for preferred rupture propagation direction. *Pure and Applied Geophysics*, *163*(2–3), 301–349. <https://doi.org/10.1007/s00024-005-0023-9>
- Escartin, J., & Cannat, M. (1999). Ultramafic exposures and the gravity signature of the lithosphere near the Fifteen-Twenty Fracture Zone (Mid-Atlantic Ridge, 14°–16.5°N). *Earth and Planetary Science Letters*, *171*(3), 411–424. [https://doi.org/10.1016/S0012-821X\(99\)00169-7](https://doi.org/10.1016/S0012-821X(99)00169-7)
- Escartin, J., Mével, C., MacLeod, C. J., & McCaig, A. M. (2003). Constraints on deformation conditions and the origin of oceanic detachments: The Mid-Atlantic Ridge core complex at 15°45'N. *Geochemistry, Geophysics, Geosystems*, *4*(8), 1067. <https://doi.org/10.1029/2002GC000472>
- Escartin, J., Mevel, C., Petersen, S., Bonnemains, D., Cannat, M., Andreani, M., et al. (2017). Tectonic structure, evolution, and the nature of oceanic core complexes and their detachment fault zones (13°20'N and 13°30'N, Mid Atlantic Ridge). *Geochemistry, Geophysics, Geosystems*, *18*(4), 1451–1482. <https://doi.org/10.1002/2016GC006775>
- Escartin, J., Smith, D. K., Cann, J., Schouten, H., Langmuir, C. H., & Escrig, S. (2008). Central role of detachment faults in accretion of slow-spreading oceanic lithosphere. *Nature*, *455*(7214), 790–794. <https://doi.org/10.1038/nature07333>
- Fletcher, J. M., Teran, O. J., Rockwell, T. K., Oskin, M. E., Hudnut, K. W., Spelz, R. M., et al. (2020). An analysis of the factors that control fault zone architecture and the importance of fault orientation relative to regional stress. *GSA Bulletin*, *132*(9–10), 2084–2104. <https://doi.org/10.1130/B35308.1>
- Früh-Green, G. L., Connolly, J. A., Plas, A., Kelley, D. S., & Grobety, B. (2004). Serpentinization of oceanic peridotites: Implications for geochemical cycles and biological activity. *The seafloor biosphere at mid-ocean ridges*, *144*, 119–136. <https://doi.org/10.1029/144GM08>
- Glink, A., & Hasenclever, J. (2024). How hydrothermal cooling and magmatic sill intrusions control flip-flop faulting at ultraslow-spreading mid-ocean ridges. *Geochemistry, Geophysics, Geosystems*, *25*(2), e2023GC011331. <https://doi.org/10.1029/2023GC011331>
- Hansen, L. N., Cheadle, M. J., John, B. E., Swapp, S. M., Dick, H. J., Tucholke, B. E., & Tivey, M. A. (2013). Mylonitic deformation at the Kane oceanic core complex: Implications for the rheological behavior of oceanic detachment faults. *Geochemistry, Geophysics, Geosystems*, *14*(8), 3085–3108. <https://doi.org/10.1002/egge.20184>
- Jian, H., Canales, J. P., Dunn, R., & Nedimović, M. R. (2024). Hydrothermal flow and serpentinization in oceanic core complexes controlled by mafic intrusions. *Nature Geoscience*, *17*, 1–6. <https://doi.org/10.1038/s41561-024-01444-y>
- John, B. E. (1987). Geometry and evolution of a mid-crustal extensional fault system: Chemehuevi Mountains, southeastern California. *Geological Society, London, Special Publications*, *28*(1), 313–335. <https://doi.org/10.1144/GSL.SP.1987.028.01.20>
- Karson, J. A., Früh-Green, G. L., Kelley, D. S., Williams, E. A., Yoerger, D. R., & Jakuba, M. (2006). Detachment shear zone of the Atlantis Massif core complex, Mid-Atlantic Ridge, 30°N. *Geochemistry, Geophysics, Geosystems*, *7*(6), Q06016. <https://doi.org/10.1029/2005GC001109>
- Kelemen, P. B., Kikawa, E., Miller, D. J., & Shipboard Scientific Party. (2007). Leg 209 summary: Processes in a 20- km-thick conductive boundary layer beneath the Mid-Atlantic Ridge, 14°–16°N. In P. B. Kelemen, E. Kikawa, & D. J. Miller (Eds.), *Proceedings of the Ocean Drilling Program, Scientific Results* (Vol. 209, pp. 1–33). Ocean Drilling Program. <https://doi.org/10.2973/odp.proc.sr.209.001.2007>
- Lay, V., Buske, S., Lukács, A., Gorman, A. R., Bannister, S., & Schmitt, D. R. (2016). Advanced seismic imaging techniques characterize the Alpine Fault at Whataroa (New Zealand). *Journal of Geophysical Research: Solid Earth*, *121*(12), 8792–8812. <https://doi.org/10.1002/2016JB013534>
- Lecoivre, A., Ménez, B., Cannat, M., Chavagnac, V., & Gérard, E. (2021). Microbial ecology of the newly discovered serpentinite-hosted Old City hydrothermal field (southwest Indian ridge). *The ISME Journal*, *15*(3), 818–832. <https://doi.org/10.1038/s41396-020-00816-7>
- Lemaux, J., Gordon, R. G., & Royer, J. Y. (2002). Location of the Nubia-Somalia boundary along the Southwest Indian ridge. *Geology*, *30*(4), 339–342. [https://doi.org/10.1130/0091-7613\(2002\)030%3C0339:LOTNSB%3E2.0.CO;2](https://doi.org/10.1130/0091-7613(2002)030%3C0339:LOTNSB%3E2.0.CO;2)
- Little, T. A., Webber, S. M., Mizera, M., Boulton, C., Oesterle, J., Ellis, S., et al. (2019). Evolution of a rapidly slipping, active low-angle normal fault, Suckling-Dayman metamorphic core complex, SE Papua New Guinea. *Bulletin*, *131*(7–8), 1333–1363. <https://doi.org/10.1130/B35051.1>
- Lukács, A., Gorman, A. R., & Norris, R. J. (2018). Quaternary structural and paleo-environmental evolution of the Alpine Fault near Haast, New Zealand, from 2D seismic reflection and gravity data. *New Zealand Journal of Geology and Geophysics*, *62*(2), 229–247. <https://doi.org/10.1080/00288306.2018.1544153>
- MacLeod, C. J., Escartin, J., Banerji, D., Banks, G. J., Gleeson, M., Irving, D. H. B., et al. (2002). Direct geological evidence for oceanic detachment faulting: The Mid-Atlantic Ridge, 15°45'N. *Geology*, *30*(10), 879–882. [https://doi.org/10.1130/0091-7613\(2002\)030<0879: DGEFOD>2.0.CO;2](https://doi.org/10.1130/0091-7613(2002)030<0879: DGEFOD>2.0.CO;2)
- MacLeod, C. J., Searle, R. C., Murton, B. J., Casey, J. F., Mallows, C., Unsworth, S. C., et al. (2009). Life cycle of oceanic core complexes. *Earth and Planetary Science Letters*, *287*(3–4), 333–344. <https://doi.org/10.1016/j.epsl.2009.08.016>
- Mével, C., Cannat, M., Gente, P., Marion, E., Auzende, J. M., & Karson, J. A. (1991). Emplacement of deep crustal and mantle rocks on the west median valley wall of the MARK area (MAR, 23°N). *Tectonophysics*, *190*(1), 31–53. [https://doi.org/10.1016/0040-1951\(91\)90353-T](https://doi.org/10.1016/0040-1951(91)90353-T)
- Mezri, L., García-Pintado, J., Pérez-Gussinyé, M., Liu, Z., Bach, W., & Cannat, M. (2024). Tectonic controls on melt production and crustal architecture during magma-poor seafloor spreading. *Earth and Planetary Science Letters*, *628*, 118569. <https://doi.org/10.1016/j.epsl.2024.118569>
- Miller, D. J., & Christensen, N. I. (1997). Seismic velocities of lower crustal and upper mantle rocks from the slow-spreading Mid-Atlantic Ridge, south of the Kane Transform Zone (MARK). In J. A. Karson, M. Cannat, D. J. Miller, & D. Elthon (Eds.), *Proceedings-Ocean Drilling Program Scientific Results* (Vol. 153, pp. 437–456). National Science Foundation. <https://doi.org/10.2973/odp.proc.sr.153.043.1997>
- Minshull, T. A., Muller, M. R., & White, R. S. (2006). Crustal structure of the Southwest Indian Ridge at 66°E: Seismic constraints. *Geophysical Journal International*, *166*(1), 135–147. <https://doi.org/10.1111/j.1365-246X.2006.03001.x>
- Mizera, M., Little, T. A., Biemiller, J., Ellis, S., Webber, S., & Norton, K. P. (2019). Structural and geomorphic evidence for rolling-hinge style deformation of an active continental low-angle normal fault, SE Papua New Guinea. *Tectonics*, *38*(5), 1556–1583. <https://doi.org/10.1029/2018TC005167>
- Momoh, E., Cannat, M., & Leroy, S. (2020). Internal structure of the oceanic lithosphere at a melt-starved ultraslow-spreading mid-ocean ridge: Insights from 2-D seismic data. *Geochemistry, Geophysics, Geosystems*, *21*(2), e2019GC008540. <https://doi.org/10.1029/2019GC008540>
- Momoh, E., Cannat, M., Watremez, L., Leroy, S., & Singh, S. C. (2017). Quasi-3-D seismic reflection imaging and wide-angle velocity structure of nearly amagmatic oceanic lithosphere at the ultraslow-spreading Southwest Indian Ridge. *Journal of Geophysical Research: Solid Earth*, *122*(12), 9511–9533. <https://doi.org/10.1111/j.1365-246X.2006.03001.x>
- Olive, J. A., Behn, M. D., & Tucholke, B. E. (2010). The structure of oceanic core complexes controlled by the depth distribution of magma emplacement. *Nature Geoscience*, *3*(7), 491–495. <https://doi.org/10.1038/ngeo888>

- Parnell-Turner, R., Escartín, J., Olive, J. A., Smith, D. K., & Petersen, S. (2018). Genesis of corrugated fault surfaces by strain localization recorded at oceanic detachments. *Earth and Planetary Science Letters*, 498, 116–128. <https://doi.org/10.1016/j.epsl.2018.06.034>
- Parnell-Turner, R., Sohn, R. A., Peirce, C., Reston, T. J., MacLeod, C. J., Searle, R. C., & Simão, N. M. (2017). Oceanic detachment faults generate compression in extension. *Geology*, 45(10), 923–926. <https://doi.org/10.1130/G39232.1>
- Parnell-Turner, R., Sohn, R. A., Peirce, C., Reston, T. J., MacLeod, C. J., Searle, R. C., & Simão, N. M. (2021). Seismicity trends and detachment fault structure at 13°N, Mid-Atlantic Ridge. *Geology*, 49(3), 320–324. <https://doi.org/10.1130/G48420.1>
- Patriat, P., & Segoufin, J. (1988). Reconstruction of the central Indian Ocean. *Tectonophysics*, 155(1–4), 211–234. [https://doi.org/10.1016/0040-1951\(88\)90267-3](https://doi.org/10.1016/0040-1951(88)90267-3)
- Picazo, S., Cannat, M., Delacour, A., Escartín, J., Rouméjon, S., & Silantiev, S. (2012). Deformation associated with the denudation of mantle-derived rocks at the Mid-Atlantic Ridge 13°–15°N: The role of magmatic injections and hydrothermal alteration. *Geochemistry, Geophysics, Geosystems*, 13(9), Q04G09. <https://doi.org/10.1029/2012GC004121>
- Picazo, S., Manatschal, G., Cannat, M., & Andréani, M. (2013). Deformation associated to exhumation of serpentized mantle rocks in a fossil Ocean Continent Transition: The Totalp unit in SE Switzerland. *Lithos*, 175, 255–271. <https://doi.org/10.1016/j.lithos.2013.05.010>
- Reston, T. J., & McDermott, K. G. (2011). Successive detachment faults and mantle unroofing at magma-poor rifted margins. *Geology*, 39(11), 1071–1074. <https://doi.org/10.1130/G32428.1>
- Robinson, A. H., Watremez, L., Leroy, S., Minshull, T. A., Cannat, M., & Corbalán, A. (2024). A 3-D seismic tomographic study of spreading structures and smooth seafloor generated by detachment faulting—The ultra-slow spreading Southwest Indian Ridge at 64°30'E. *Journal of Geophysical Research: Solid Earth*, 129(9), e2024JB029253. <https://doi.org/10.1029/2024JB029253>
- Sandiford, D., Brune, S., Glerum, A., Naliboff, J., & Whittaker, J. M. (2021). Kinematics of footwall exhumation at oceanic detachment faults: Solid-block rotation and apparent unbending. *Geochemistry, Geophysics, Geosystems*, 22(4), e2021GC009681. <https://doi.org/10.1029/2021GC009681>
- Sauter, D., Cannat, M., Rouméjon, S., Andreani, M., Birot, D., Bronner, A., et al. (2013). Continuous exhumation of mantle-derived rocks at the Southwest Indian Ridge for 11 million years. *Nature Geoscience*, 6(4), 314–320. <https://doi.org/10.1038/ngeo1771>
- Schroeder, T., Cheadle, M. J., Dick, H. J., Faul, U., Casey, J. F., & Kelemen, P. B. (2007). Nonvolcanic seafloor spreading and corner-flow rotation accommodated by extensional faulting at 15°N on the Mid-Atlantic Ridge: A structural synthesis of ODP Leg 209. *Geochemistry, Geophysics, Geosystems*, 8(6), Q06015. <https://doi.org/10.1029/2006GC001567>
- Schroeder, T., & John, B. E. (2004). Strain localization on an oceanic detachment fault system, Atlantis Massif, 30°N, Mid-Atlantic Ridge. *Geochemistry, Geophysics, Geosystems*, 5(11), Q11007. <https://doi.org/10.1029/2004GC000728>
- Schuck, B., Schleicher, A. M., Janssen, C., Toy, V. G., & Dresen, G. (2020). Fault zone architecture of a large plate-bounding strike-slip fault: A case study from the Alpine Fault, New Zealand. *Solid Earth*, 11(1), 95–124. <https://doi.org/10.5194/se-11-95-2020>
- Searle, R. C., Cannat, M., Fujioka, K., Mével, C., Fujimoto, H., Bralée, A., & Parson, L. (2003). FUJI Dome: A large detachment fault near 64°E on the very slow-spreading southwest Indian Ridge. *Geochemistry, Geophysics, Geosystems*, 4(8), 9105. <https://doi.org/10.1029/2003GC000519>
- Sieh, K. E. (1978). Slip along the San Andreas fault associated with the great 1857 earthquake. *Bulletin of the Seismological Society of America*, 68(5), 1421–1448. <https://doi.org/10.1785/BSSA0680051421>
- Smith, D. K., Cann, J. R., & Escartín, J. (2006). Widespread active detachment faulting and core complex formation near 13°N on the Mid-Atlantic Ridge. *Nature*, 442(7101), 440–443. <https://doi.org/10.1038/nature04950>
- Smith, D. K., Escartín, J., Schouten, H., & Cann, J. R. (2008). Fault rotation and core complex formation: Significant processes in seafloor formation at slow-spreading mid-ocean ridges (Mid-Atlantic Ridge, 13–15°N). *Geochemistry, Geophysics, Geosystems*, 9(3), Q03003. <https://doi.org/10.1029/2007GC001699>
- Smith, D. K., Schouten, H., Dick, H. J., Cann, J. R., Salters, V., Marschall, H. R., et al. (2014). Development and evolution of detachment faulting along 50 km of the Mid-Atlantic Ridge near 16.5°N. *Geochemistry, Geophysics, Geosystems*, 15(12), 4692–4711. <https://doi.org/10.1002/2014GC005563>
- Theunissen, T., & Huisman, R. S. (2022). Mantle exhumation at magma-poor rifted margins controlled by frictional shear zones. *Nature Communications*, 13(1), 1634. <https://doi.org/10.1038/s41467-022-29058-1>
- Tucholke, B. E., Lin, J., & Kleinrock, M. C. (1998). Megamullions and mullion structure defining oceanic metamorphic core complexes on the Mid-Atlantic Ridge. *Journal of Geophysical Research*, 103(B5), 9857–9866. <https://doi.org/10.1029/98JB00167>